Seismic Sensitivity Analysis of Different Carbonate Lithofacies: a Full-elastic Simulation

MASTER OF APPLIED EARTH SCIENCE THESIS

Davis Farish

April 1st 2015

Supervisor: Dr. Stefan M. Luthi

Advisor: Runhai Feng

TU Delft Delft University of Technology

Faculty of Civil Engineering and Geoscience
Department of Applied Earth Sciences

Title	:	Seismic Sensitivity Analysis of Different Carbonate Lithofacies: a Full-elastic Simulation

Keywords	:	Reservoir evaluation, carbonates, seismic, forward modelling, full-waveform inversion, reservoir characterization, full-elastic

Author(s)	:	D.R. Farish

Date	:	Publicly defended on August 24th, 2015
Professor(s)	:	Dr. S.M. Luthi
Supervisor(s)	:	Dr. S.M. Luthi, R. Feng

Postal Address : Section for Applied Geology
Department of Geoscience & Engineering
Delft University of Technology
P.O. Box 5028
The Netherlands
Telephone : (31) 15 2781328 (secretary)
Telefax : (31) 15 2781189

Acknowledgements

I would like to first start off by thanking Evert Slob and others involved for accepting me as a student to TU Delft and giving me the opportunity to pursue a Master of Science. Thanks again to Evert who did not give up on me and was willing to help me formulate my Free Master's Program even though it was sometimes a pain to deal with the administration. I would then like to thank Stefan Luthi for agreeing to take me on as another Masters student even though he was very busy and gave me the opportunity to do a MSc. Thesis in applied geology. Thank you for the hard work you put into supervising me throughout the 9 months. Thank you to Stefan's PhD student, Runhai Feng, for teaching me how to use the programs required for the thesis as well as always being available and willing for consultation when I was having technological difficulties. Thank you to Dries Gisolf at Delft Inversion for providing the algorithms which were utilized in this thesis and permitting me to use them.

I would also like to thank my mother, father, and grandfather for all the support and encouragement both during my bachelors and Master's programs. There is no way that I would be who I am and where I am today without them. To my girlfriend Linnéa who dealt with being across oceans during my studies and also for living with me in Delft during the end, thanks for the support!

Lastly, thank you to all my friends in the Applied Geophysics program whom I had amazing times with, the Petroleum Engineers in Delft who I spent long hours with in the field, and the geologist in Zürich for hosting great events.

Abstract

Using a complete 2D full-elastic seismic simulation from geological modelling, to 2D seismic data forward modelling, to non-linear full-waveform inversion – the interaction of various carbonate lithofacies are observed. Specifically, three different environments of deposition within a carbonate shelf along with their pore-types ranging from partially cemented moldic macropores, open vugs, to the intergranular pores of coral facies are of key interest. To fully grasp the interaction, lithofacies determination of the inverted parameters are characterized to see if the different lithofacies can be matched to their true counterpart of the geological model or distinguishable based on crossplot clustering. In the end, our findings show that individual pore-types are unable to be detected using only inverted surface-seismic data – rather, various facies groups of depositional environments are capable of being characterized by the crossplot clustering of elastic parameters and seismic velocities.

Table of Contents

Table of Figures

List of Tables

1. Introduction

There are many sedimentary obscurities left confined within the boundaries of geology and geophysics. As a result, earth scientists around the world aim to capitalize on the potential to further public knowledge by unveiling the mysteries that await via their own scientific research. This thesis intends to do just that; with respect to the focus of petroleum reservoir geology this research aspires to aid in the acceleration of peak oil further into the future by means of helping the exploration and production (E&P) industry discover prospects which were previously thought unobtainable as well as increase oilfield productivity. Specifically, the focus of this research lies within the domain of carbonate reservoirs. E&P efficiency could potentially be improved by having a better method of differentiating between diverse carbonate lithofacies prior to spending the millions of dollars necessary to appraise them with exploration wells.

We have seen an amplified interest in carbonates due to techniques that were initially developed to characterize sandstone reservoirs that are now being applied to carbonate reservoirs around the world. As such, carbonate rocks will be the primary focus for this thesis due to the increased oil and gas production of lacustrine and deep-water environments which were deemed as “potential reservoirs” but have turned out, in some cases, to be very prolific. Lacustrine sediments are now major oil producers in places such as the Unita Basin (Utah), China, and Brazil. Likewise, deep water limestones have turned out to be productive in several areas within the North Sea basin and in North America (Scholle, et al., 1983). On top of these new reservoirs being produced, the giant Middle East carbonates contain around 50% of the world’s oil and have been in production for almost a century (Schlumberger, 2007).

However, like any new endeavor carbonates present unique challenges and technical risks that must be probed and understood. Unlike their sedimentary relatives’ siliciclastics (sandstones and conglomerates) which create some of the best petroleum reservoirs in the world, carbonate rocks have a complex texture and pore network which exist contained within different carbonate lithofacies. More specifically, facies which have roughly the same percentage of porosity (the capability of a rock to hold fluids in pores) but still have different acoustic properties. Intergranular pores in the midst of rounded grains or secondary pores such as moldic and vuggy pores are examples of these. It is well known that there is a vast difference between the two types of pores when it comes to producing hydrocarbons from them. This is due to differences in permeability, which is the capability of a rock to transmit a fluid between its pore connections. Thus, the uncertainty arises within the E&P sector of interpreting between these two pore types on a seismic section; one pore type would lead to high profits during production while the other type may want to be avoided all together depending on the producer. As a result, better porosity measurements have long been a focus for research among geoscientists. For example, quite a bit of research has been devoted to understanding the differences in acoustic properties such as shear modulus, bulk modulus, and density between the different pore types but most analysis has been observed through the use of sonic acoustic velocity. With that said, the objective of this thesis is to determine whether the differences in acoustic properties such as shear strength or incompressibility between these carbonate lithofacies are noticeable enough to be detected within the realm of exploration scale seismic resolution.

1.1 Carbonates

Carbonates are sedimentary rocks deposited in mostly marine environments with clear, shallow, warm waters since deposition often takes place on marine shelves in waters that do not have high mud supplies. The most common carbonate rock, limestone, which will be the carbonate facies of this study originates by three main processes: (1) precipitation of calcium carbonate in an initially stony condition, as in travertine (mineral springs) and organic reefs; (2) lithification of calcium carbonate sediments, which includes selective dissolution of matrix and/or grains, precipitation of mineral cement in pore spaces, and may end with recrystallization; and (3) replacement of calcium sulfate or quartz by calcium carbonate (Harbaugh, 1967). In addition, limestones are grouped broadly into three major environmental suites: (1) nonmarine environments from large inland structural basins (lakes and alluvial fans); (2) shallow-water marine and/or marginal marine environments (beaches, lagoons, bays, dunes, etc.); and (3) open-sea environments (Lønøy, 2006). One of the most important aspects of carbonate deposition is that much of the material has biogenic components made up by fragments of marine organisms, skeletons, coral, mollusks, and algae consisting of mostly precipitated calcium carbonate which is chemically active. In addition, there are many non-skeletal components which make up carbonate grains such as ooids, peloids, and mud. All of these unique grains (skeletal & non-skeletal) are important because once the carbonate rock is formed, a range of chemical and physical processes begin to alter the rock structure changing fundamental characteristics such as porosity and permeability. This is known as diagenesis (Schlumberger, 2007). Different diagenetic processes include: cementation, micritisation, neomorphism, dissolution, compaction/fracturing, and dolomitization (Weltje, 2013). These diagenetic processes are paramount due to their creation of heterogeneities at all scales within the reservoir and unique pore types. In particular, the cementation and dissolution processes continuously modify the pore structure to create or destroy porosity (Eberli, et al., 2003).

For the finer porosity details, carbonate pore types can be separated into four groups: (1) connected porosity formed during deposition (primary porosity), which exist in the midst of carbonate grains or crystals known as intergranular and intercrystalline respectively; (2) vugs and moulds, which are unconnected pores resulting from dissolution of calcite cement by water during post deposition diagenesis (secondary porosity); (3) fracture porosity which is caused by stresses following deposition; and (4) sucrose dolomite porosity (resulting from replacement of calcite by dolomite) (Harbaugh 1967, Schlumberger 2007). Even though pore types such as sucrose dolomite porosity are crucially important in reservoirs such as the Devonian rocks of the west Texas Permian Basin, the two pore types which will be analyzed during this research of non-fractured limestones are intergranular and moldic/vuggy which can be seen in Figure 1 (Harbaugh, 1967).

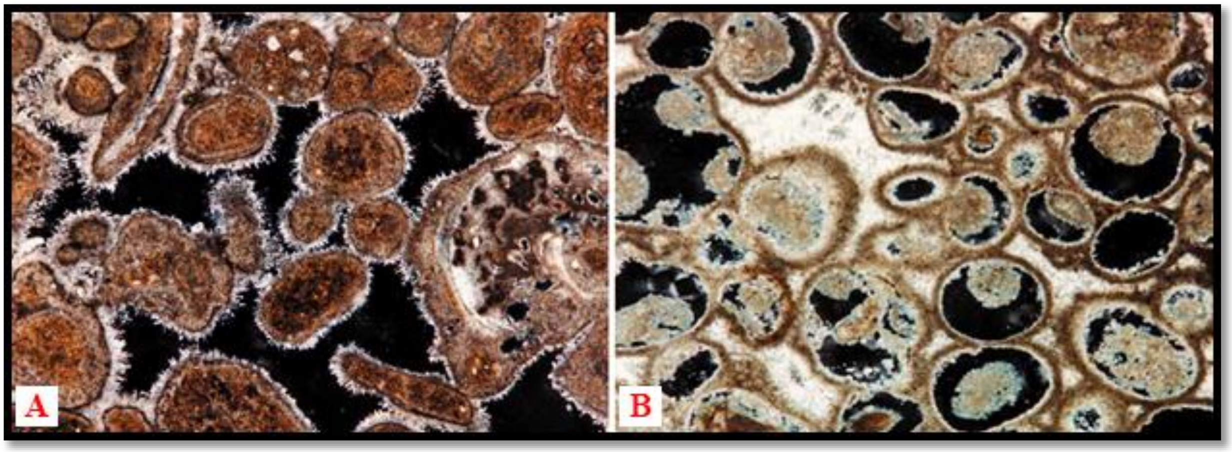

Figure 1: Microscopic images of ooid intergranular porosity (A) and moldic porosity of dissolved ooid grains (B). (Weltje, 2013)

Intergranular porosity predominates after deposition of a sediment when grains form a loose package with little cementation (Anselmetti, et al., 1993). These Interparticle pores are normally associated with medium-to-high-energy depositional settings in the studied data set, such as rimmed, platform-margin shoals, distally steepened ramp-margin shoals, inner-ramp fringing shoals, middle-ramp barrier shoals, local platform interior shoals, gravity-driven flow deposits, beaches, wash-over fans, and others (Lønøy, 2006).

On the contrary, moldic pores are divided into two natural classes on the basis of intramold pore sizes: moldic micropores and moldic macropores. The pores are commonly associated with partially dissolved or recrystallized peloids, ooids, and foraminifera with microgranular structure. Both diagenesis and depositional setting control the macromoldic porosity distribution. Mineralogically unstable grains, e.g., aragonite and evaporite minerals, are commonly more susceptible to dissolution than the surrounding calcitic or dolomitic matrices. In regard to vuggy porosity, many vugs are simply solution-enlarged molds where the outlines of the precursor grains are poorly defined. The pores are of irregular size and shape and may or may not be interconnected (Lønøy, 2006).

1.2 Elastic Properties

When one refers to “seismic” in respect to hydrocarbon exploration, it is meant that the properties of sound are exploited when interacting with a rock in the subsurface. More specifically, the velocity of sound is different for each rock it encounters. This resulting contrast in acoustic impedance (bulk density multiplied by velocity) for different lithological boundaries generates energy and some of it is reflected back to and recorded at the earth's surface. Physically speaking, sound is a wave which can occur in several ways but in the petroleum industry, only the P- and S-waves (illustrated in the Figure 2) are exploited. P-waves, or compressional/push waves, behave like a spring or a slinky that would be 'pushed' through the matter. S-waves, or shear waves, move in an up and downward motions as you can imagine waves on the surface of the sea behave. The shearing of the S-wave only occurs if the neighboring section of the medium can be "pulled" by the propagating wavefront. As one could imagine, a "neighbor" within a fluid substance cannot be pulled upward in comparison to a solid material simply because it behaves as a liquid. Therefore in fluids, S-waves do not exist while in a solid both P- and S-waves can be transmitted (Drijkonigen, 2009).

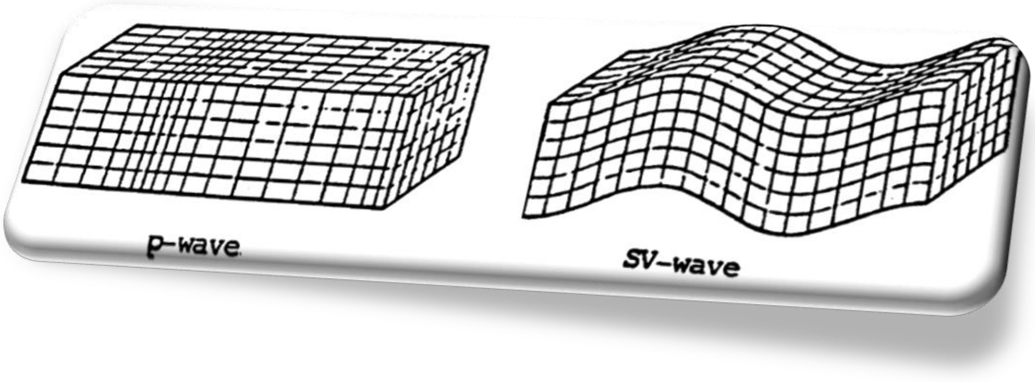

Figure 2: Motion of the acoustic P-wave and vertical S-wave (courtesy of Drijkonigen, 2009).

As the P- and S-wave propagate through the subsurface of the earth, the earth reacts elastically to the small but rapid deformations caused by the transient seismic pulse (Ghose, et al., 2013). That is, the earth is subtly deformed but quickly returns to the same state previous to distortion. As such, the degree of elasticity/plasticity of earth material depends mainly on the strain rate, i.e., the length of time it takes to achieve a certain amount of distortion. The lower the strain rate a material can achieve the more ductile that material can be described as. In addition, within its elastic range the behavior of the earth material can be described by Hooke's Law that states that the amount of strain is linearly proportional to the amount of stress. Beyond its elastic limit the material may either respond with brittle fracturing (e.g., earthquake faulting) or ductile behavior/plastic flow.

The resistivity to stress a material demonstrates can be quantified by various elastic moduli. The first of these is, bulk modulus (K), which is defined as the ratio of the hydrostatic pressure change to the resulting relative volume change. In other words, it is a measure of the material's resistance to change in volume, or incompressibility. In relation to P-wave velocity (V_p) and S-wave velocity (V_s) bulk modulus can be written as:

$$\mathrm{K} = \rho\left(\frac{{V_p}^2 - 4{V_s}^2}{3}\right) \qquad [1]$$

Next, shear modulus (μ), or rigidity, is a measure of the resistance of the material to shearing, i.e., to changing the shape and not the volume of the material. Since true liquid has no shape, fluids (including gases) have a shear modulus of zero. On the other hand for solid material of very strong resistance, shear modulus approaches infinity. It can be expressed as:

$$\mu = \rho \cdot {V_s}^2 \qquad [2]$$

Finally, Poisson's ratio (σ), is the ratio between the lateral contraction (relative change of width) of a cylinder being pulled on its ends to its relative longitudinal extension. The dynamic Poisson's ratio can be obtained from the relation of V_p/V_s:

$$\sigma = \frac{\frac{Vp^2}{Vs^2} - 2}{2\left(\frac{Vp^2}{Vs^2} - 1\right)} \qquad [3]$$

Missing from this list of elastic moduli is Young's modulus because it will not be applied in this paper (Ghose, et al., 2013).

With that said, the higher the rigidity (shear modulus μ) of the material, the higher the P- and S-wave velocities will be. Rigidity usually increases with density of a material which explains why denser rocks have normally faster wave propagation velocities (Ghose, et al., 2013). Even so, the factors which are causing the change of the shear modulus are not well understood, but earth scientists suggest a connection to the pore types. Indeed, it is well established that pore type variations cause compressibility variations at any given porosity which certainly emphasizes the importance of pore type when it comes to velocity prediction (Baechle, et al., 2005). Furthermore as previously alluded, S-waves must travel through the contact of grains through a rock. Thus, a purely solid rock with zero cracks or pores will have much higher seismic velocity than that of an unconsolidated gravel or a highly fractured facies. This is also true for P-waves even though they can travel through fluid and not only grain contacts. For this reason, velocity usually increases with subsurface depth as the rocks get more compacted resulting in the closure of cracks and pores from the overburden lithostatic pressure.

As one could surmise by now, the uniqueness of carbonates comes from the pore type being almost equally important in the elastic behavior and resultant P- or S-wave velocities. Consequently unlike in siliciclastic sediments – compaction, burial depth, and age are less important factors for acoustic velocity in carbonates. In addition, aside from rock density and effective stress, the most important medium properties that affect seismic velocities (especially for carbonates) are porosity, cementation, and fluid saturation.

In regard to cementation, the degree to which grains in a carbonate rock are cemented together by post depositional diagenesis has a strong effect on the effective elastic moduli. By filling pore space with minerals of higher density than the fluid it replaces – the bulk density is increased. The combination of porosity reduction and cementation causes the observed increase of velocity with depth of burial and age (Ghose, et al., 2013). In regard to fluid saturation, when S-wave (shear) velocity encounters a saturated rock, either dispersion can occur or the shear can take a preferential propagation path which avoids altered (weakened) section (Adam, et al., 2006). This is why different velocities in rocks with equal porosities are the result of different pore types and thus, velocity is strongly dependent on the rock-porosity. For example, increase in porosity produces a decrease in velocity – this relation can be examined in Figure 3 below. In addition, velocity differences at equal porosities can be over 2500 m/s, especially at higher porosities. For example, moldic rocks with porosities of 39% can have $V_p's$ between 2400 m/s and 5000 m/s. Even at porosities of less than 10% the velocity can still vary about 2000 m/s, which is an extraordinary range for rocks with the same chemical composition and the same amount of porosity. Likewise, porosity can vary widely at any given velocity. Rocks with a V_p of 4100 m/s can have porosities anywhere between 12%-43% (Eberli, et al., 2003). To have a better understanding of this relation, refer to the research presented by Eberli et al. (2003) in Figure 3.

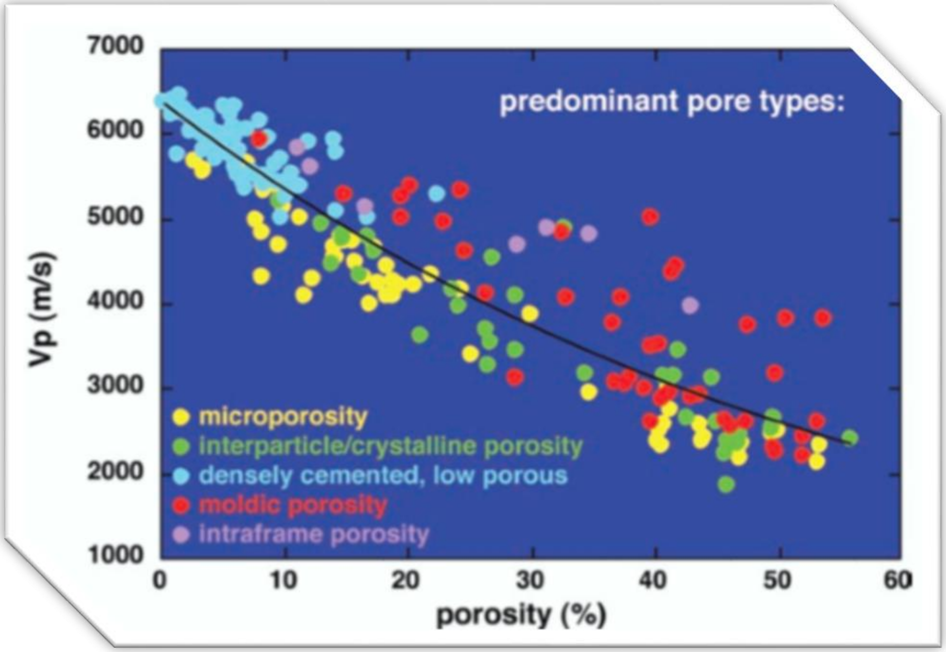

Figure 3: Graph of velocity (at 8 MPa effective pressure) versus porosity of various pore types of carbonates. The two main pore types of interest are the green (Interparticle) pores and the red (moldic) pores. (Eberli, et al., 2003)

In a facies with intergranular pore types the S-wave will encounter fluid saturation and must "snake" around the different grain contacts of the rock in order to propagate through it. Thus, the accumulation of loose grains and crystals of that such as a dolomitized limestone results in a low velocity. In comparison, the frame-forming pore types (moldic and vuggy) result in significantly higher velocity values than do pore types that are not embedded in a frame such as intercrystalline and intergranular pores (Eberli, et al., 2003). For moldic/vuggy porosity, the S-wave is allowed to traverse a much quicker propagation path throughout the cement and micrite surrounding the porous grains. This pre-compaction cementation which occurs in the shallow subsurface of some moldic rocks changes the elastic behavior by increasing the stiffness via a framework of cement around the moulds. As a result, a significant increase in acoustic velocity is instigated which is far greater than the velocity increase due to compaction from lithostatic pressures (Eberli, et al., 2003). The travel time through this framework is faster than through grains that are only connected by point contacts, as found in rocks with intergranular porosity (Anselmetti, et al., 1993). For example, as perceived in Figure 3, rocks with moldic porosity between 40-50% can have V_p's between 4000 and 5000 m/s, which is extraordinarily high for porous rocks and much higher than their intergranular counterparts (Eberli, et al., 2003). However, it should be realized that the increase in porosity that is associated with the appearance of moldic and vuggy porosity can partly block the propagation of wave fronts (Soete, et al., 2014).

Nevertheless, do all of these differences in elastic moduli between carbonate pore-types consistently show up on exploration scale seismic sections and full-waveform inversion? This is the basis for the research and it is expected that seismic indicators alone will not be enough and that lithofacies determination techniques post-inversion will have to be employed. Even then, it is likely that the pore-types will be too far in the zone of subseismic resolution for characterization.

2. Literature Review with Dataset

Prior to achieving any synthetic acoustic data simulation, quantitative parameters such as P-wave velocity, S-wave velocity, and bulk density must be collected to describe the geological architecture and rock facies being propagated by the seismic wavelet. Instead of collecting new seismic data in the field or modelling an observable outcrop, pre-existing literature pertaining to elastic properties of carbonate rocks as well as carbonate depositional environments was reviewed. Much of the theory was shared in subchapters 1.1 and 1.2; but in addition to what was covered, real velocities pertaining to the three carbonate pore types as well as different depositional settings had to either be created or sought out. As such, rather than handpick certain velocities within a reasonable range to match each individual facies within the geological model, actual velocity measurements from a paper published in 2014 were utilized after reviewing several potential datasets. It was fortunate for the sake of this study to come across “Pore space evolution and elastic properties of platform carbonates” by Francois Fournier et al. (2014) which contains a dataset of 214 ultrasonic “dry-rock” velocity measurements at five different effective pressures. The samples were taken from a limestone of the Lower Cretaceous platform carbonates located in various localities belonging to Southeast France. The samples had a total porosity ranging from 0.1% - 23.1% and were thoroughly classified into five groups of dominant pore types: 1) intercrystalline micropores; 2) intergranular macropores; 3) open moldic macropores; 4) partially cemented moldic macropores; and 5) open vugs (2-5 also contain small amounts of intercrystalline micropores) (Fournier, et al., 2014).

From these 214 samples, roughly twenty samples were extracted to be used as good candidates for this research. The criteria for selecting said samples included having a porosity of at least 10-20%, the samples’ facies association, and having the correct dominant pore type. The first porosity association mentioned above (intercrystalline microporosity) was excluded from the selection because it does not lie within the area of interest for this study. With that said, the twenty samples in Table 1 below represent the available pool which was used to populate the final model with different values and the nine highlighted samples are those which were chosen. In Chapter 3 – “Geological Modelling” – contains a brief explanation of why these nine samples were selected. Lastly, it should be noted all P- and S- wave velocities are for 10 MPa effective pressure.

Petrophysical Laboratory Measurement Samples

Sample Number	Pore Type	Porosity (%)	V_p (m/s) 10 MPa	V_s (m/s) 10 MPa	Texture/facies Association
1	Intergranular	12.8	5156	2826	Packstone/rudist facies
2	Intergranular	13.9	4588	2513	Rudstone
3	Intergranular	9.9	5170	2828	Packstone/calcarenitic
4	Open moldic	23.1	3787	2155	Rudstone
5	Open moldic	21.9	3800	2143	Rudstone
6	Open moldic	12.8	5072	2772	Grainstone/rudist
7	Open moldic	11.6	5485	2941	Wackestone/rudist
8	Open moldic	19.9	4351	2422	Rudstone
9	Partially cemented moldic	12.5	4782	2657	Rudstone
10	Partially cemented moldic	16.8	4588	2476	Rudstone
11	Partially cemented moldic	17.2	4955	2730	Rudstone
12	Partially cemented moldic	18.7	4533	2531	Grainstone/coral facies
13	Partially cemented moldic	12.8	5214	2826	Wackestone-floatstone/rudstone
14	Partially cemented moldic	15.4	4766	2648	Packstone/rudstone
15	Partially cemented moldic	11.4	5491	3028	Grainstone/rudstone
16	Partially cemented moldic	10.7	4960	2726	Grainstone/rudstone
17	Partially cemented moldic	19.3	4531	2422	Rudstone
18	Open vugs	12.1	5568	2964	Wackestone/rudstone facies
19	Open vugs	10.9	5591	3026	Wackestone/rudist
20	Open vugs	10.5	5700	3170	Rudstone

Table 1: A table of the 20 samples chosen from the 214 available as candidates to use for the geological model with the 9 highlighted samples being the ones chosen for the geological model. All sample measurements were executed by Fournier et al. (2014) during their research, “Pore space evolution and elastic properties of platform carbonates”.

Aside from reviewing literature for a dataset to use, research on depositional environments and potential carbonate reservoirs was completed in order to theorize a worthy geological model. In the end, several 2D analogues from the book Carbonate Depositional Environments written by Shoelle et al. (1983) were used as references for the model. A carbonate shelf and resulting fore-reef slope environment was selected as it was suspected that the carbonate shelf environment would perhaps be the best candidate to represent all rock textures and pore types needed for the experiment.

Carbonates can be deposted in a wide range of marine environments. When refering to oceaninc carbonates, there are at least four different ways they can typically be characterized: 1) carbonate ramps; 2) carbonate platforms; 3) carbonate banks; and 4) pelagic deepwater carbonates (Weltje, 2013). These categrories are represented in the Figure 4 diagram to the right.

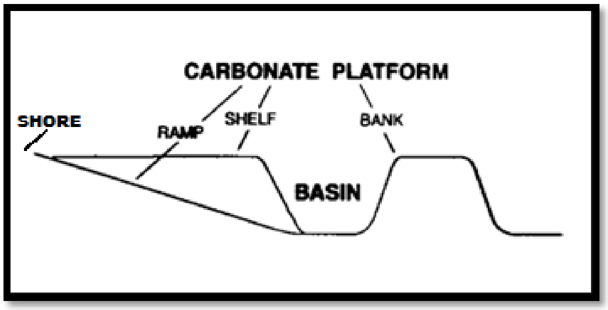

Figure 4: The four marine deposition environments for carbonates: ramp; shelf; bank; and deep-water extending right.

Carbonate shelves are deposited in low-energy, shallow-water bays or lagoons and then are accreted seawards. An example formation of a carbonate shelf would be comprised of patch reefs, mud mounds, and carbonate-sand (oolite) shoals (Scholle, et al., 1983). Low-energy environments, such as the back reef shoals, which are protected from wave and current action, are characterized by higher concentrations of lime mud while clean rocks with high original permeabilities are found in high-energy zones at the shoreline or around the main reef wall. If the basin area associated with either of these sections generates hydrocarbons the oil and gas should migrate up the structure (shoreward) into the porous carbonate rocks (Nurmi, et al., 1997). For a 3D representation of this shallow water carbonate shelf and sequential fore-reef slope, refer to the model created by Schlumberger Limited (1997) (Figure 5).

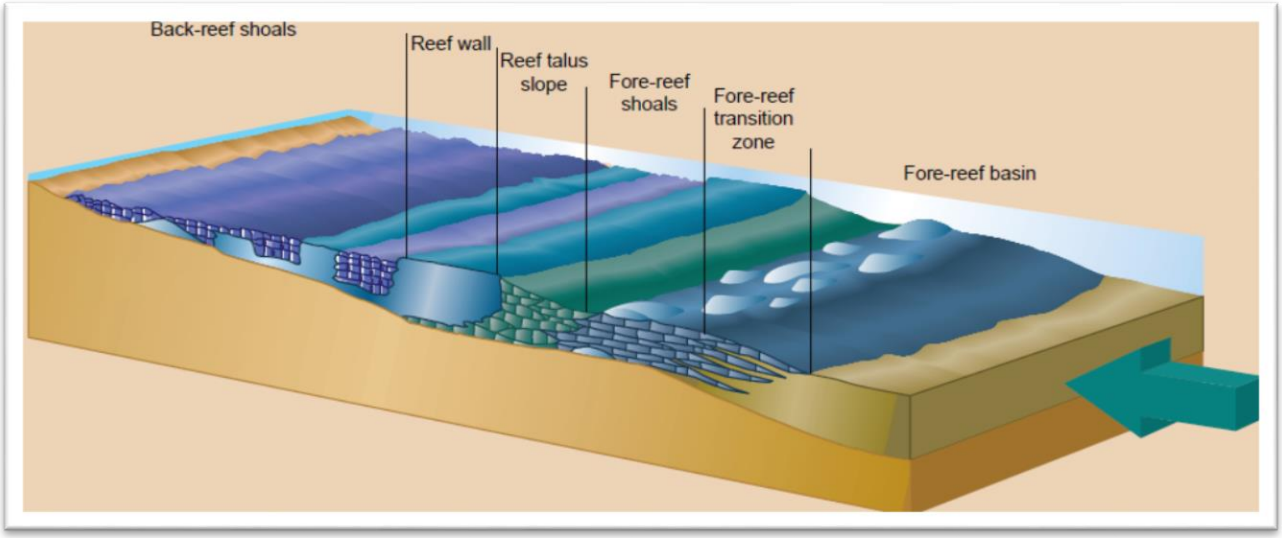

Figure 5: A carbonate shelf and fore-reef slope environment depicting the various oolite shoal and reef facies that can be present. The green arrow represents the direction in which hydrocarbons from the basin would migrate. (Nurmi, et al., 1997)

A fore-reef slope is understood to be gravity induced deposits located seaward of reef-rimmed carbonate shelves or platforms. The particles originate from shallow-water carbonate environments and consist of transported reef and shelf debris mixed and interbedded with basinal-mud deposits (Scholle, et al., 1983). The reef of the uppermost part of the fore-reef slope is the main region of economic potential in hydrocarbon exploration. This is partly due to the location being at the edge of a basin, wherein most of the hydrocarbon charge is generated and migrates upward toward the potential reef reservoir. Reefs are composed of coarse skeletal grains with framework support and generally high permeability. Indeed, this is the intergranular porosity as discussed in Chapter 1.1 in which we hope to distinguish during the seismic simulation. A detailed 2D image of a fore-reef slope is illustrated in Figure 6 and the following figure represents a possible fore-reef slope that has been exposed in Morocco (Figure 7).

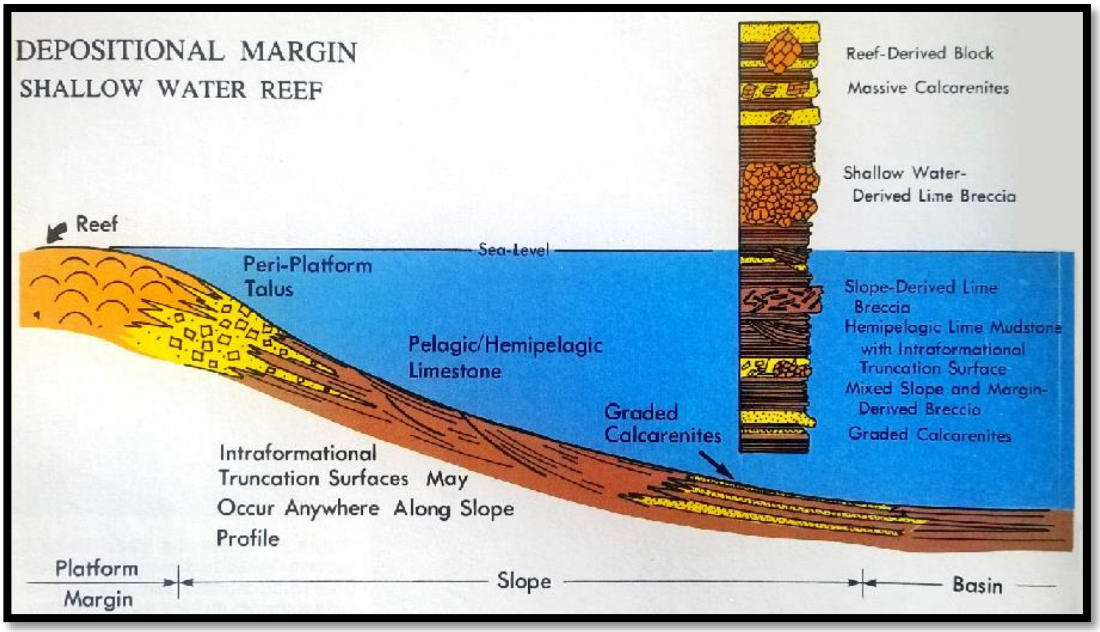

Figure 6: Deposition of a shallow water fore-reef slope extending down into the basin. After burial, potential hydrocarbons charged in the basin would potentially migrate up toward the carbonate reef. (Scholle, et al., 1983)

Figure 7: A geological feature in central Morocco suspected to be a core-reef-complex (top) and sequential fore-reef slope which after numerous years of erosion has been exposed at the surface. The lateral scale of the unit is approximately 4-5 kilometers wide.

3. Geological Model

The geological model is a representation of the Earth's natural subsurface and is described by a set of model parameters (velocities, densities, etc.). In order to properly investigate parameter sensitivities of different carbonate lithofacies a realistic geological model must be formed. As mentioned in Chapter 2, the model which was designed is based generally on the interpretations of depositional environments by Sholle et al. (1983). Figure 8 is a 2D illustration of what the carbonate shelf environment would look like during the actual deposition and Figure 9 resembles what it could look like post-lithification.

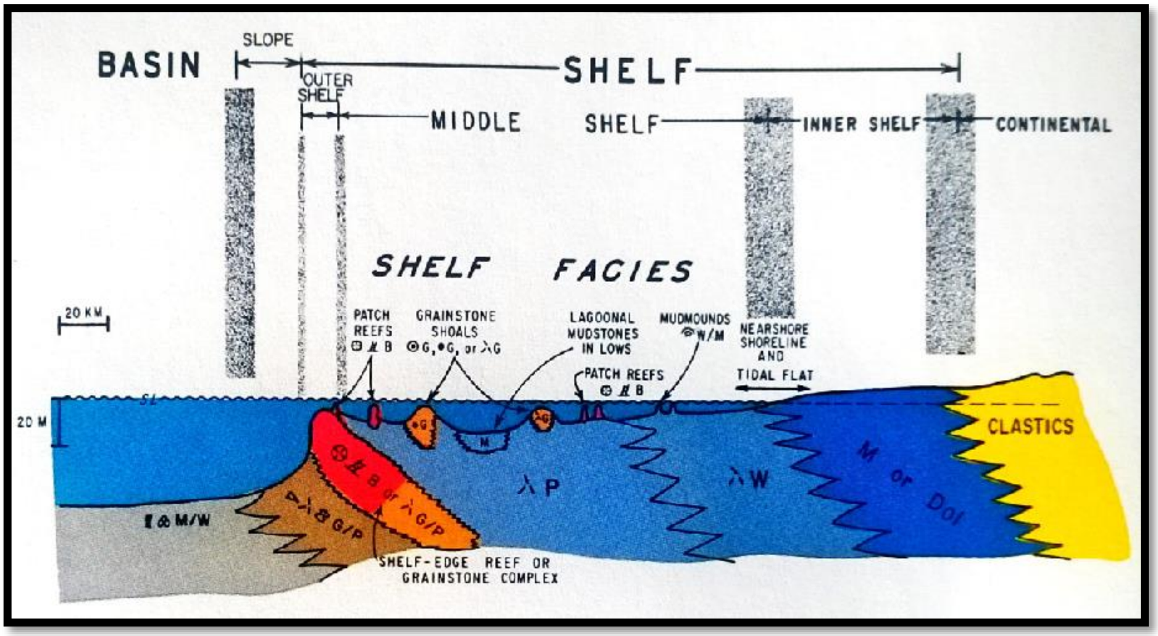

Figure 8: A carbonate shelf facies with the continental sandstones on the far right transitioning to the inner shelf, middle shelf, outer shelf, and fore-reef slope. (Scholle, et al., 1983)

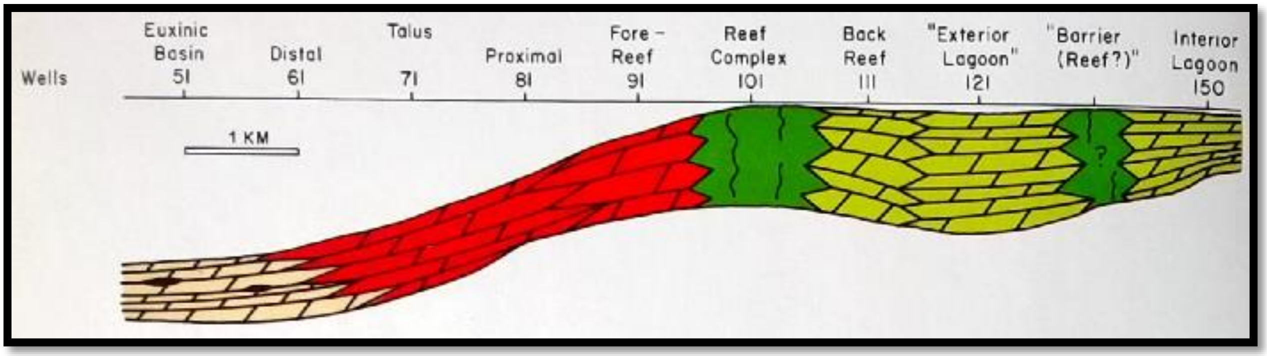

Figure 9: Illustration of a carbonate shelf and fore-reef slope after being solidified and cemented. (Scholle, et al., 1983)

Initially, the geological model was hand sketched several times and the nine highlighted samples from Table 1 were assigned to different facies. The samples were allocated based on a realistic assumption of the percentage of porosity present in each facies as well as their pore type. Subsequently, a base model was created and can be seen in Figure 10 which was created in Microsoft paint. The carbonate rocks have clastic shale layers above and below them (dark blue) and the section is 500 m tall while the lateral extent is 12.5 km. Thin layers of shale with different

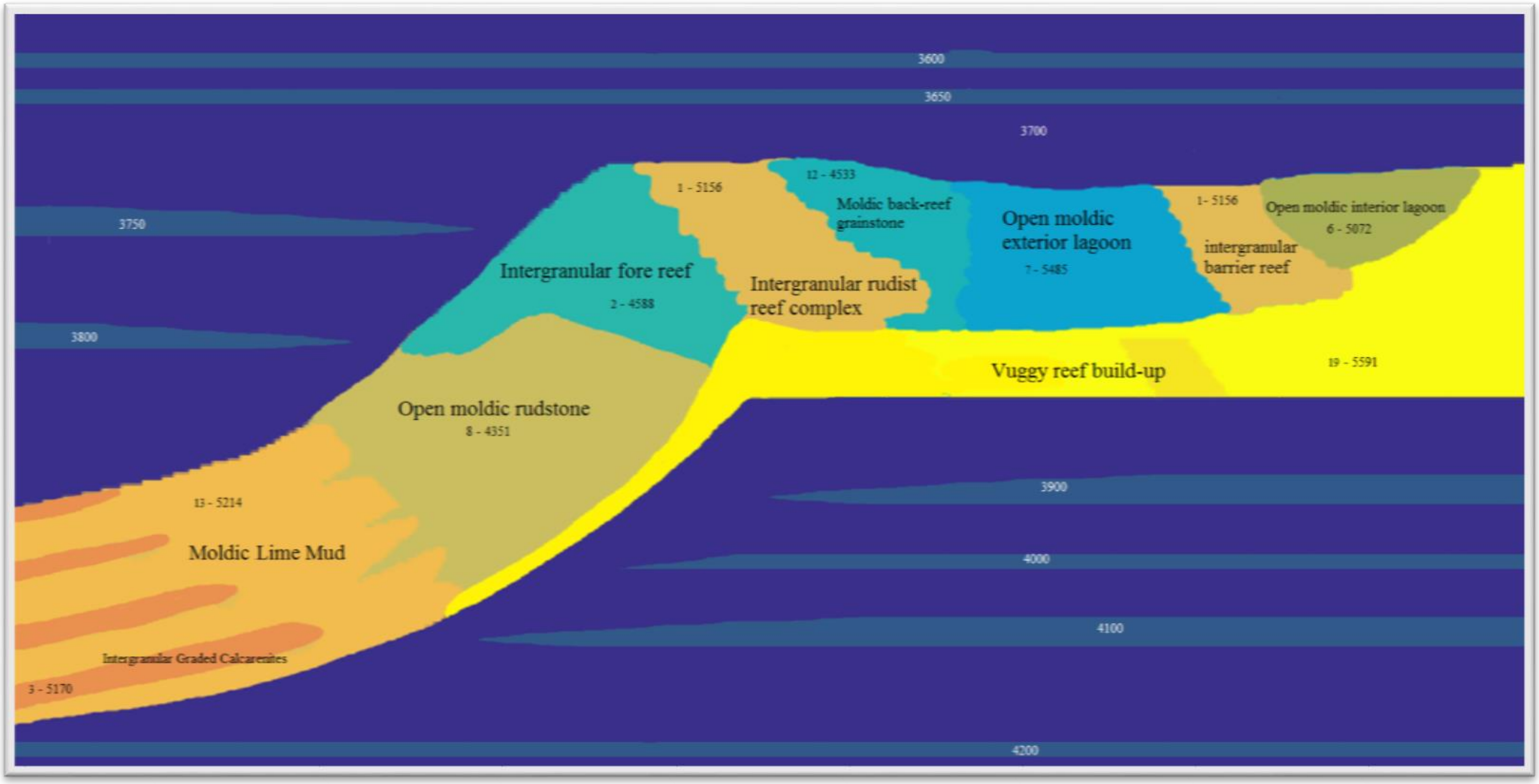

Figure 10: Base geological model of a carbonate shelf and fore-reef slope with shale above and below in dark blue. The section is theoretically 500 m tall and 12.5 km wide. The values within the model correspond to the sample numbers from Table 1 and P-wave velocity (m/s) respectively. In addition, it can be seen that each unit has a facies and pore type description.

velocities were grafted in the model in order to create multiple reflection for the inversion process. In an example of the facies allocation, facies number seven from Table 1 was assigned to the exterior lagoon of Figure 10 because it is a non-cemented mud-supported wackestone with low porosity of 11.6%. This sample facies matches because deep lagoons have very low energy (quiet water) regions that quite often build up wavy-bedded mudstones/wackestones with low porosity and permeability. The wavy-bedding is created by microbial or algal mats; a thin sheet of biofilm which rests on the surface. Moreover, due to the low energy environment of the lagoon circular ooids are able to exist without being washed away. These ooids are composed of calcium carbonate and after lithification of the carbonate facies the calcite is dissolved away to create the secondary open moldic porosity. It should be noted that not all samples may perfectly align with the corresponding facies of the geological model as a very quick and concise allocation was performed based on the existing knowledge and limited number of samples the student had at the time.

Next, in order to create the genuine digital model (Figure 11, Figure 12, and Figure 13), the software Matlab was utilized in which the model was drawn and the program populated the geometric features with values – thus creating three 250 by 500 matrices populated with V_p, V_s, and bulk density. The dimensions of the matrices were made relatively small in order to minimize the processing times in both the forward and inverse problems (Chapters 4 and 5) due to the limited time of this thesis.

For this model, the bulk density (ρ) for each facies was calculated by the equation

$$\rho = (1 - \phi) * \rho_g \qquad [4]$$

where ϕ is the porosity of said facies and ρ_g is grain density. 2.71 g/cm^3 was used for grain density as it is median value for marine carbonate rocks. As one might notice, since these samples were lacking bulk density values initially and the loose equation [4] was used to calculate all of them, this could potentially be a problem when inverting for densities in the later installments of this research since seismic inversion for density data is already difficult to begin with. For example when using this equation, facies number one, six, and thirteen from Table 1 will all have the same density of 2363 kg/m^2 due to them having the same porosity of 12.8% even though they are of different pore and facies association – which is highly unlikely.

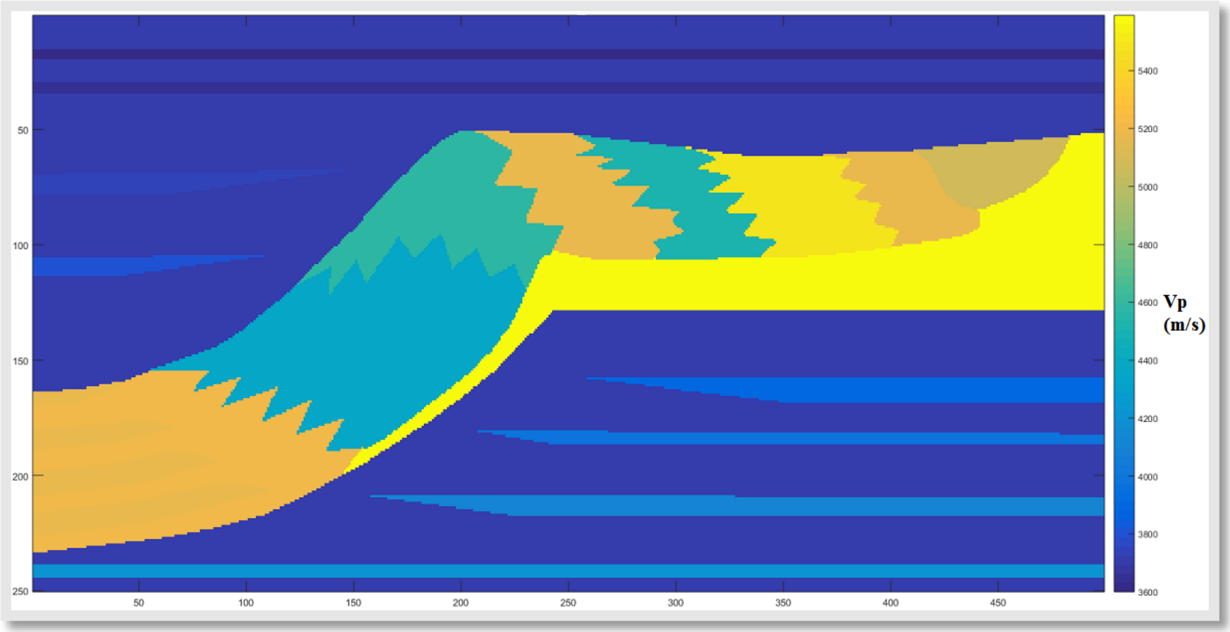

Figure 11: Visual representation of base geological model populated with P-wave velocity values.

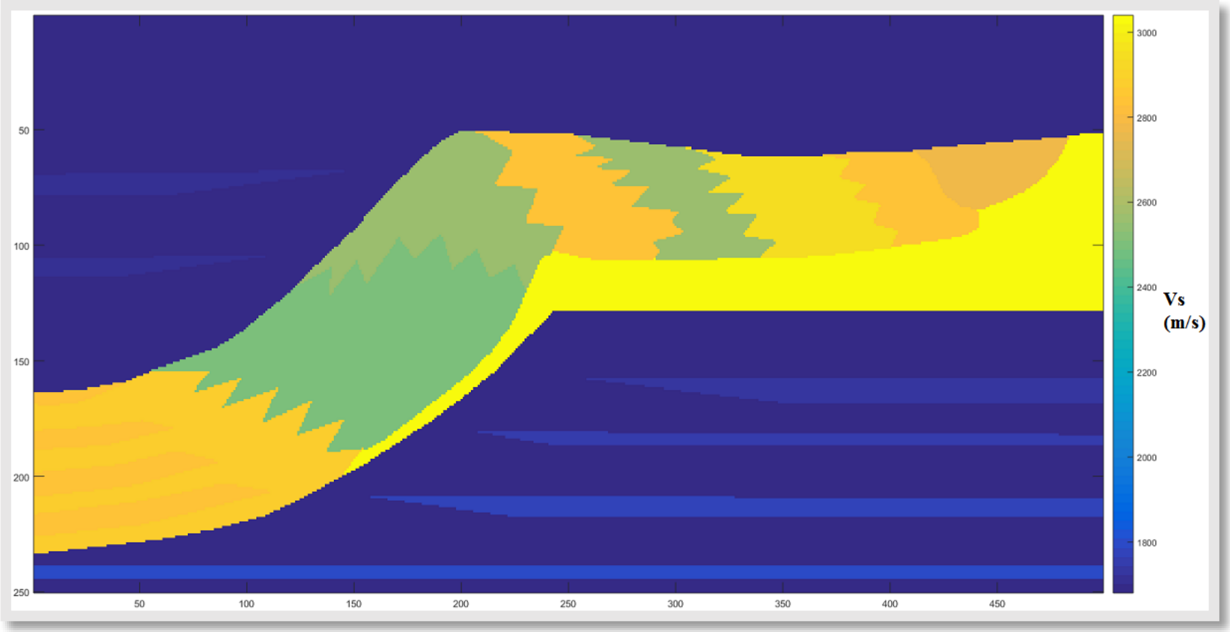

Figure 12: Visual representation of base geological model populated with S-wave velocity values.

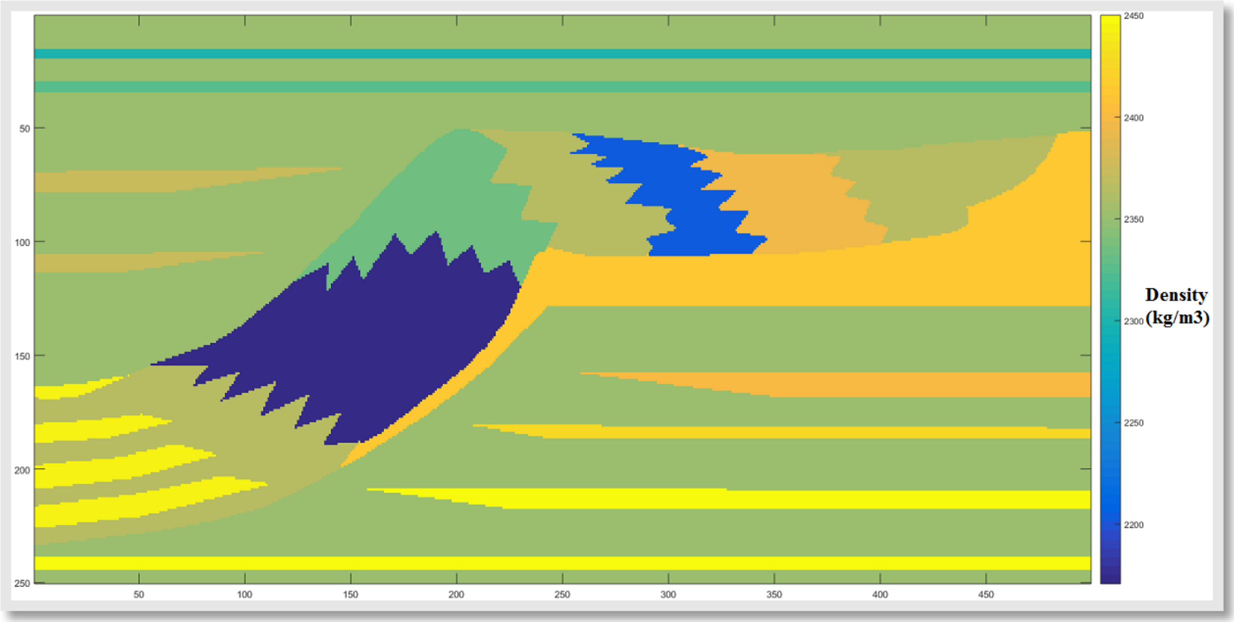

Figure 13: Visual representation of base geological model populated with density values.

4. Seismic Forward Modelling

The main task of geophysics is to study physical properties and processes within the solid Earth. However, generally one cannot directly access the regions of interest (e.g. hydrocarbon reservoir) within the subsurface. Therefore, indirect methods have to be employed, such as estimating material properties or physical process parameters from geophysical signals captured with appropriate sensors to eventually create an image (Maurer, 2014). However, occasionally when going out into the field, capturing the response of a controlled source via sensors is not an option be it for lack of time or equipment. Thus, enters seismic forward modelling (as applied in this research) for method used to synthetically generate data which would resemble what a geophysicist would gather during a real surface-seismic exploration venture. Forward modelling can thus be used as a replacement for field acquisition during research or the geophysicist can use both as a comparison and quality assessment before and/or after the acquisition.

In the field, the seismic signal which was reflected from the subsurface (e.g. hydrocarbon reservoir) is processed in order to determine a model representing the geological structure of the subsurface (Sirgue, 2003). Indeed, this is the reason why carbonate data samples are grafted into a digital geological model (see Chapter 3) so that we may have a theoretical ‘subsurface’ to perform such experiment. When mimicking this forward process on computer modelling software, the laws of physics (e.g. the seismic wave equation) allow us to simulate the action and interaction of physical parameters for a given subsurface model; this process is known as the ‘forward problem’. For this study the geological model which contains a set of petrophysical parameters, once excited by a pulse of acoustic energy, synthesizes a set of measureable quantities: the data which represents the forward model (Sirgue, 2003; Tetyukhina, 2010).

This geophysical data space is an observation that has a finite number of measurement positions typically dictated by logistics, financial resources available, or in this case processing power. Furthermore, seismic observations include a time series of ground displacement, velocity, or acceleration as a function of position and time. As a result, the data comes out as a so-called seismogram complete with travel times and amplitudes. In the end, forward modelling provides useful insights into the nature of a geophysical problem by estimating data for a given set of model parameters (Maurer, 2014). Furthermore, when applied to well-known geological models, seismic forward modeling provides insights into those geological features that can be observed on actual seismic data as well as increase the awareness of seismic artifacts (Tetyukhina et al., 2011).

4.1 Synthetic Data Simulation

The forward modelling method used in this paper is the Kennett invariant embedding method (Kennett, 1983). The method is exact and unlike finite difference methods does not suffer from numerical dispersion effects (Tetyukhina et al., 2011). The method as applied in this research uses a 2 m vertical discretization of the input model parameters, with the calculation incorporating all internal multiple reflection and transmission effects. This factor of 2 vertical discretization was applied to create a realistic reservoir thickness; given that the geological model has 250 rows the forward model thus has a maximum of 500 m depth as it is sampled $(250 \cdot 2)$ times in the vertical axis. As a result, this makes the entire carbonate package ~160 m thick. On the horizontal axis, the program samples a common-midpoint (CMP) seismic trace every 25 m over 500 columns of the geological model. Indeed this is equivalent to shooting a seismic source every 25 meters for 12.5 km $(500\ shots \cdot 25$ m spacing).

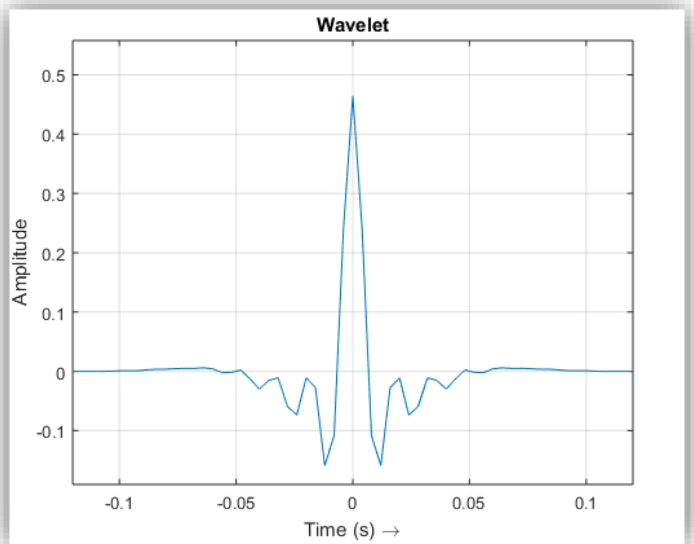

Figure 14: A zero-phase band-pass filter wavelet with corner frequencies 6 – 12 – 60 - 75 Hz which was applied to the forward modelling process.

For each location (500 in total), a set of ten incident plane waves with angles ranging from 0-80% degrees of the critical angle at the highest P-wave velocity in the entire section are obtained. Figure 15 shows an example of these ten incident plane waves for five different (CMP) shot locations. Furthermore, the synthetic seismic data generated was obtained using a one-dimensional (1D) model for each of these 500 surface traces; such combinations of a 1D subsurface model with a 2D wavefield are known as 1.5D models. The wavelet utilized is a zero-phase band-pass filter wavelet with corner frequencies 6 – 12 – 60 – 75 Hz and is shown in Figure 14. In addition, the time sampling rate of the traces is 4 milliseconds and random white noise is added to the data for realism (Tetyukhina et al., 2011).

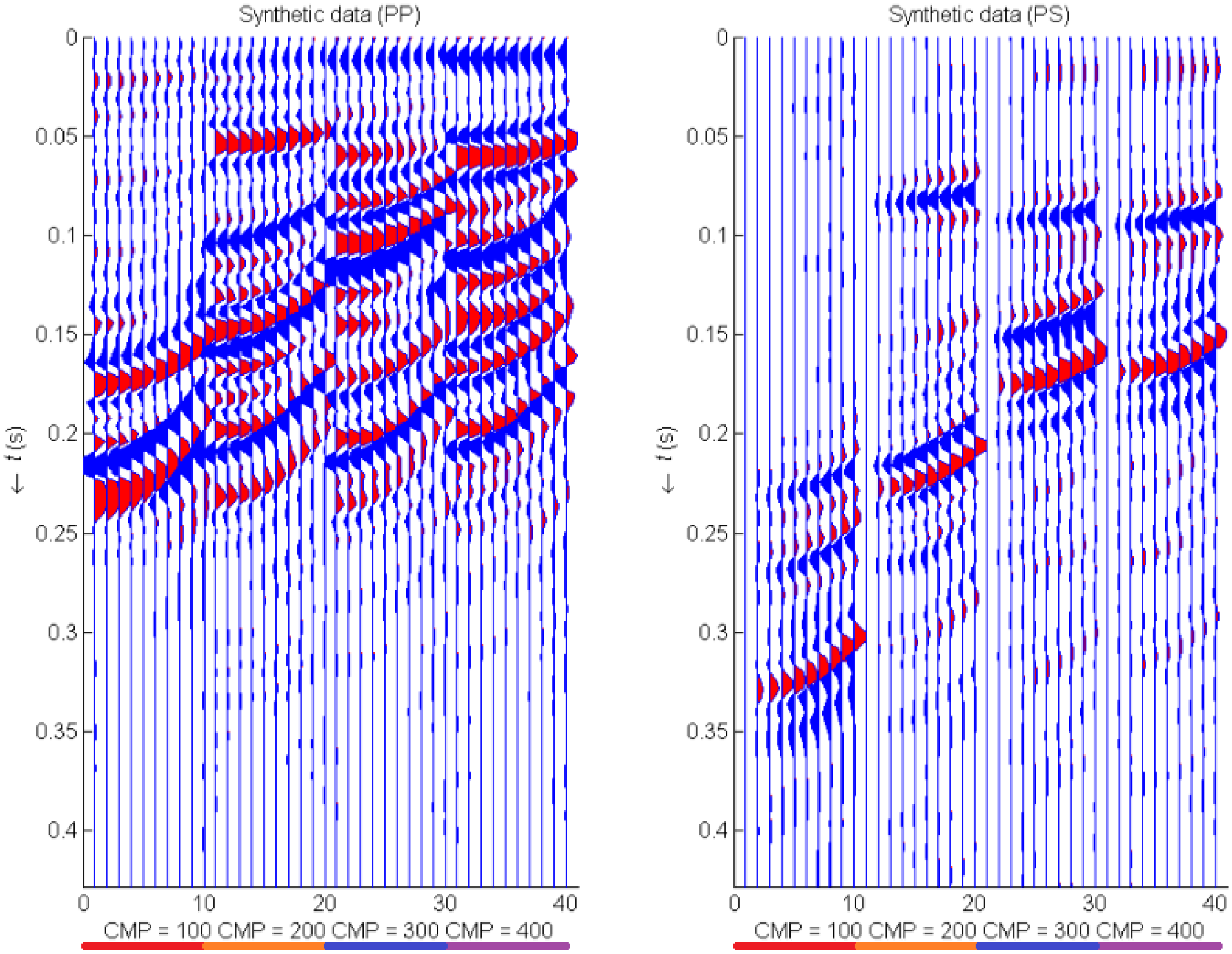

Figure 15: Synthetic data computed in the Radon (τ/p) domain (time vs. horizontal slowness). For each (CMP) location a set of 10 incident plane waves with angles ranging from 0-80% degrees of the critical angle at the highest P-wave velocity in the entire section were obtained. However, in this figure only (CMP) shot locations 100, 200, 300, and 400 are represented as an example with each color representing corresponding CMP line on Figure 16. The left hand side shows the synthetics generated for P-waves while the right side is S-wave.

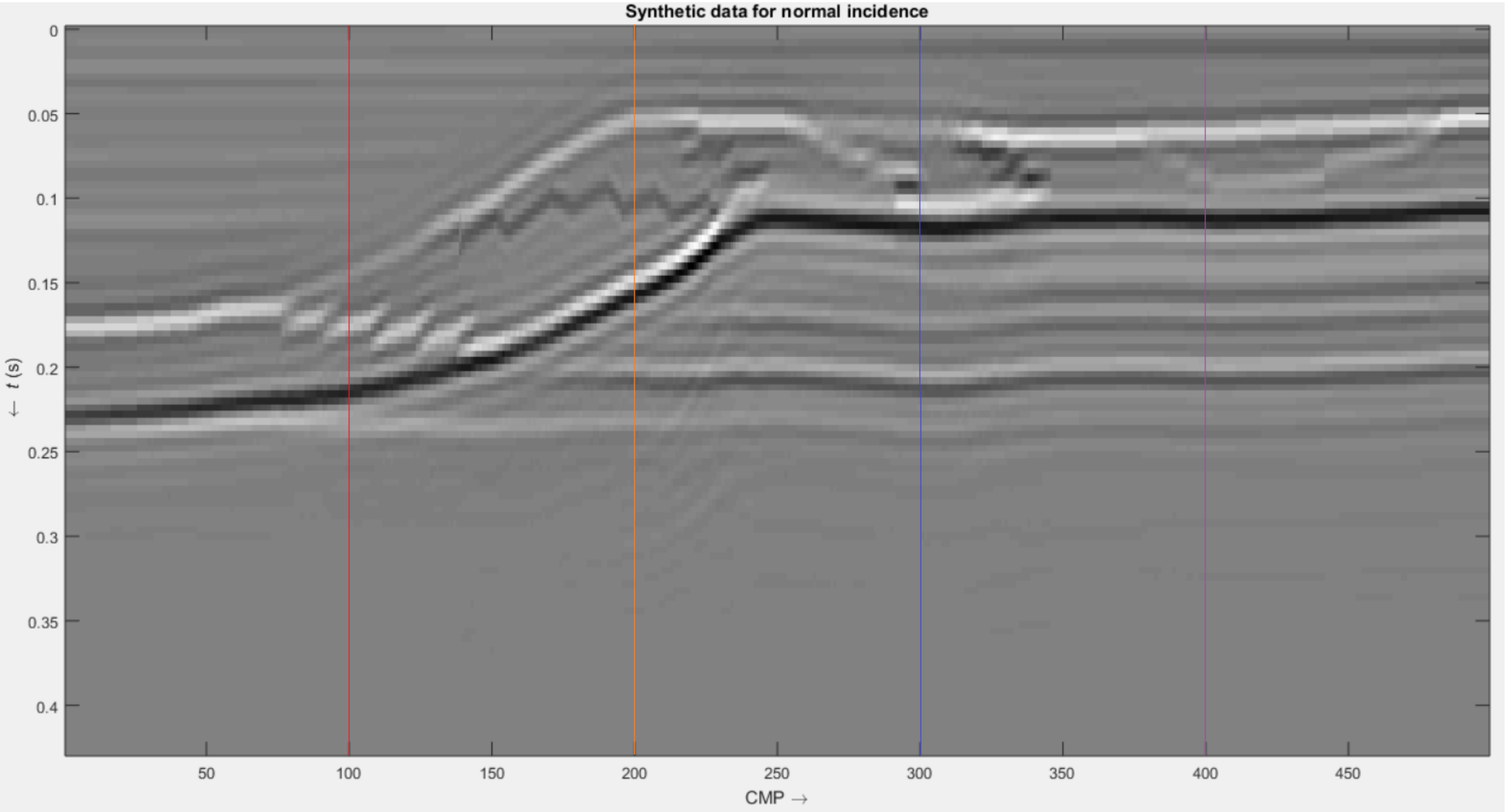

Figure 16: Synthetic forward modelling seismic data created by the Kennett invariant embedding method. The different colored lines correspond to the four synthetics represented on Figure 15.

Figure 16 displays the synthetic results that were obtained with the parameters mentioned above. However, this figure is only for normal incident plane waves, that is, shots that were simulated as if the source shot and sensor were on top of each other. For display purposes, the synthetic data created with ten incident angles as opposed to normal incidence will not be displayed.

It can be seen that all major geometries of the geological model have been clearly resolved. As a result, a geologist would easily be able to interpret this time-series synthetic seismogram to be a carbonate shelf platform and fore-reef slope. Due to the simplicity of the model and these geometries being so clearly resolved, the interpreter would easily be able to pick out the core-reef complex or fore-reef as the main areas of interest for drilling hydrocarbons. However, the aim of this thesis is not to distinguish the different carbonate pore-types by their geometries but instead (in the case of forward-modelling) by the acoustic nature of geological interfaces. As such, it can be determined that in this forward model the different pore-type lithofacies are not distinguishable by any sort of seismic indicators (i.e. contrasting amplitudes) on the seismogram and they would not be interpretable without the known geometries of the carbonate structure as a whole. Although the facies at CMP location 300 is a bit more dim on the top depositional surface of the shelf, it can be seen on Figure 15 that CMP 300 just below 0.05 seconds does not have a contrasting amplitude but a positive (red) amplitude on the PP data just like the other CMP locations. Usually a dim spot such as this is a direct indicator of hydrocarbons but since these rocks are unsaturated not much can be inferred.

5. Non-linear Full-waveform Inversion

As no lithology estimation could be conjectured from the synthetic full elastic wavefield model in Chapter 4.1 other than by the geological structure itself, the attention is now shifted to obtaining quantitative information in hopes of characterizing the reservoir. The method addressed here is full-waveform inversion for reservoir characterization (FWI-res) and the forward model which was created can be applied to this method. Full-waveform inversion is a powerful tool within the geophysical arsenal and ultimately, we as geophysicists are interested in the determination of model parameters from observed data (Maurer, 2014).

The process of determining subsurface properties and finding a model that best explains a set of measured/observed data is identified with the solution of a so-called 'inverse problem' (Tetyukhina, 2010; Maurer, 2014). The inverse problem is a growing body of theory and with the ever increasing computer processing power the improvement of geophysical inversion methods continue to grow. Until the early 1960's, geophysical inversion was carried out almost exclusively and qualitatively within the geophysicist's brain (Tetyukhina, 2010). Since then, quantitative algorithms based on the seismic wave equation or one of its numerous approximations have been developed to enable the inversion of measured data for the desired subsurface characteristics. The 'inverse problem' thus applies the opposite of the 'forward problem', where the aim is to reconstruct a model of the subsurface from a set of given measurements (observations) (Tetyukhina, 2010). Figure 17 illustrates this relationship between the inverse and forward problems.

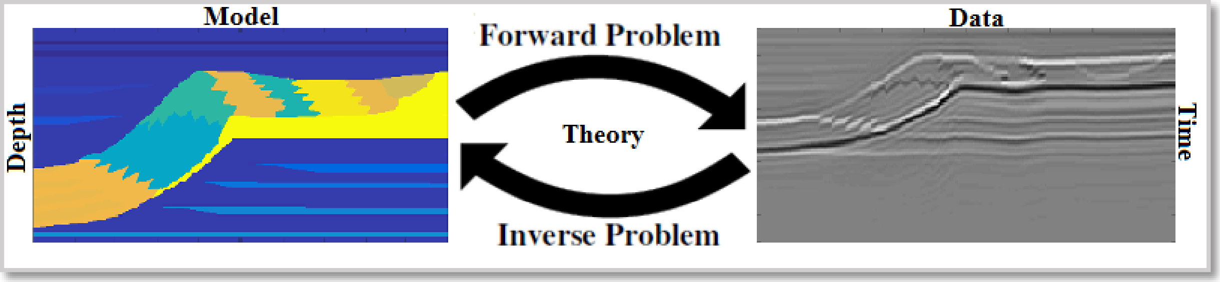

Figure 17: The Inverse and the Forward Problem in inversion. The inverse problem seeks to estimate a depth model of the desired subsurface property (most often velocities and densities) from seismic data recorded in the field or simulated on computer software (courtesy of Sirgue, 2003).

As it is, there are three main ingredients of inverse theory, namely (i) observed data, (ii) unknown material properties, and (iii) physical relationships between the data and the unknown model parameters (Maurer, 2014). The forward problem was seen in Chapter 5 to create observed data. The geological model on the left side of Figure 17 was used which represents the true earth and then the seismic response data was derived as a function of time. For the inverse problem, the geological model is theoretically unknown (ingredient ii) and the only properties that are known about the subsurface come from the observed data on the right side of Figure 17 as well as a minute amount of *a priori* information. Information which is *a priori* (Latin phrase for what comes before) refers to previous knowledge, in this case of the subsurface, which is often a velocity model derived from analyzing the data. However, this research instead uses a 'background' model which will be discussed later in this chapter. The fundamental problem with having only observed data and *a priori* to work with is that when applying the inverse problem, the answer may be estimated and thus differs from the true geological model. This is in part due to the forward modelling process providing us with incomplete information on the model. In addition, the forward problem is only an approximation and the model is a simplified representation of the true system. To make matters even more complicated, the observed data is recorded by tangible instruments in the field and thus contain noise (or noise is added in the simulation for realism) making the data inconsistent and messy often messy (Sirgue, 2003).

In the circumstance of this research, the subsurface property estimation which is desired is that of three elastic moduli (V_p, V_s, and density) coming from signals in the seismographs that are generated by the forward modelling process (Maurer, 2014). The process which produces such estimations is the FWI-res method as mentioned previously; this algorithm was developed by Gisolf and van den Berg (2010) from Delft University of Technology. The inversion is full-waveform elastic meaning that the scheme takes the full wave into account. This includes internal multiple scattering, transmission effects and mode conversions, normally considered as noise in linear inversion but become essential signals in FWI-res (Haffinger et al., 2015). The full-waveform approach allows for the recovery of broadband properties and provides a high resolution (Gisolf et al, 2014). However, the inversion does not allow for frequency inversion which only serves the purpose of improving the background velocity model for migration. Rather, it utilizes the full bandwidth of the data and yields property images at a commensurate resolution (Gisolf, et al., 2010).

As touched upon previously, the FWI-res strategy is based on the scattering theory in which the wavefield propagation is calculated in the inhomogeneous media (Gisolf, et al., 2014). Consequently, the technology delivers three elastic properties on a high-resolution grid, driven by the physics only, and avoiding any user-imposed constraints (Haffinger et al., 2015). However to develop that end result, the well-known P- and S- velocities are broken down into true elastic properties, notably the compressibility $\kappa = \frac{1}{\mathrm{K}}$ (inverse of bulk modulus K) and the shear compliance $\mathrm{M} = \frac{1}{\mu}$ (inverse of shear modulus μ). For a review on these elastic properties and how they are derived from V_p and V_s refer to sub-chapter 1.2. What was not mentioned in this sub-chapter is the relation to κ and μ to P- and S-wave velocity; the equations are as follows

$$V_P = \sqrt{\frac{1}{\rho}(\frac{1}{\mathrm{K}} + \frac{4}{3M})} \tag{5}$$

$$V_S = \sqrt{\frac{1}{\mathrm{M}\rho}} \tag{6}$$

However, κ, M and ρ are not the values inverted for in the FWI-res scheme; rather the true properties are restated in terms of normalized ‘contrasts’ against the ‘background’ reference mediums (κ_0, M_0, and ρ_0) which are to be solved instead

$$\chi_{\kappa}(z) = \frac{\kappa(z) - \kappa_0(z)}{\kappa_0(z)} \tag{7}$$

$$\chi_{\mathrm{M}}(z) = \frac{\mathrm{M(z)} - \mathrm{M_0(z)}}{\mathrm{M_0(z)}} \tag{8}$$

$$\chi_{\rho}(\mathrm{z}) = \frac{\rho(\mathrm{z}) - \rho_0(\mathrm{z})}{\rho_0(\mathrm{z})} \tag{9}$$

Contrast equations [7, 8 and 9] are considered 1.5-D approximations due to the contrasts only being functions of the local depth variable z. It should be well understood that the definition of the contrast functions is based on the difference between the background medium and the true properties. In comparison, the definition of reflectivity is based on the difference between the true properties across a boundary (Haffinger, 2013). This method of using inhomogeneous background models allows for the exploitation of reducing the contrasts sufficiently enough to allow for proper linearization. The significance in this comes from the idea that in the subsurface the possibility exists for the contrast between two media to be too large for linearization of the problem. Thus, this would result in the inaccuracy of predicting wavefields (Lam et al., 2006).

These background models κ_0, $\mathrm{M_0}$ and ρ_0 as perceived in Figure 18 represent the best *a priori* information which is available before the inversion process but what exactly are these backgrounds? In a field application of a geophysical survey, the true properties are not available so the geophysicist would normally have to rely on processing of the data to obtain velocities. For example, the background would come from the macro-model, also known as the velocity model. The velocity model is generated from a processing technique that uses stacked velocity analysis in which the velocities are defined from the normal moveout (NMO) of the reflection hyperbola in the seismogram (Yilmaz, 1987). The stacking velocities are then converted to interval velocities using Dix's formula (Dix, 1955; Sirgue, 2003). As for the background in bulk density, it would have to come from regional well control data or gravity measurements (Tetyukhina et al., 2014). However, in the FWI-res method the backgrounds are space-variant and smooth models which are obtained from highly smoothing the true κ, M and ρ models. During the smoothing process, the incident wavefields (characterized in space and time by an impulse, called a delta Dirac function) and Green's functions are calculated (Gisolf et al., 2014; Ghose, et al., 2013). These Green's functions represent the elastic impulse response of the background medium generated by all

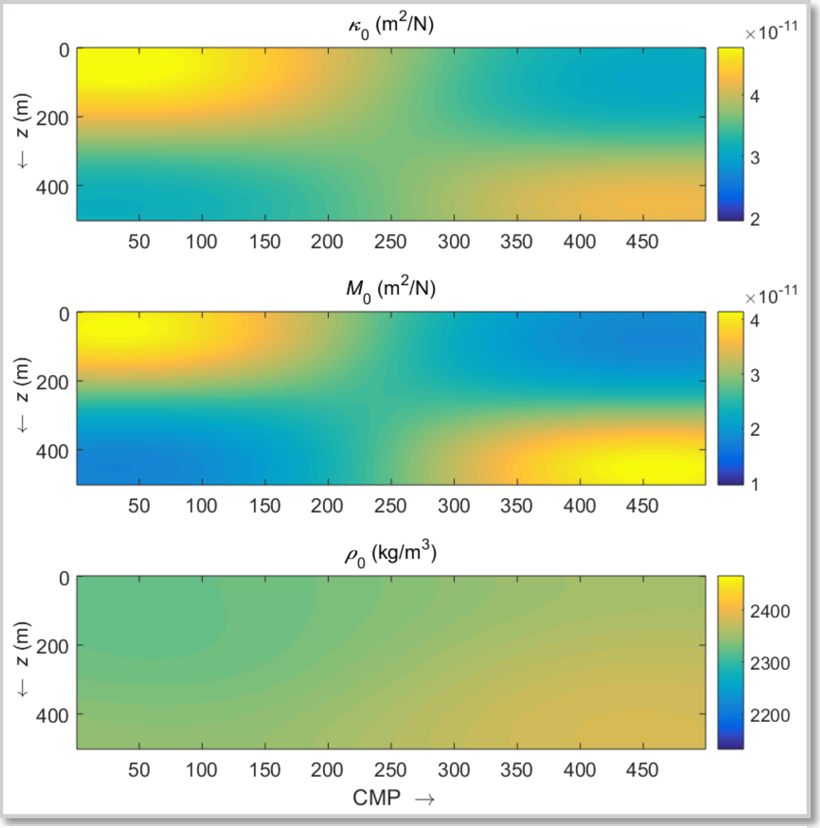

Figure 18: Smooth background models in terms of compressibility κ, shear compliance M, and density ρ. The backgrounds represent the best knowledge of these elastic parameters before the inversion process. A high cut filter of 5 Hz was applied to the backgrounds.

different types of elastic sources. Thus, the backgrounds roughly describe the kinematics of the data and represent the best knowledge of the elastic parameters before the inversion (Gisolf et al., 2014). By using these simple background models as seen in Figure 18, the (FWI-res) method requires limited user input as opposed to conventional inversion schemes making it more of a “hands-off” approach. As an effect, the results will be more objective (Veeken et al., 2014). Figure 19 shows an example from CMP 400 where the true property values are shown in blue as a function of local depth, z (in meters). The red curves represent the background which will be used for the inversion and it can be seen that they are highly smoothed versions of the true parameters.

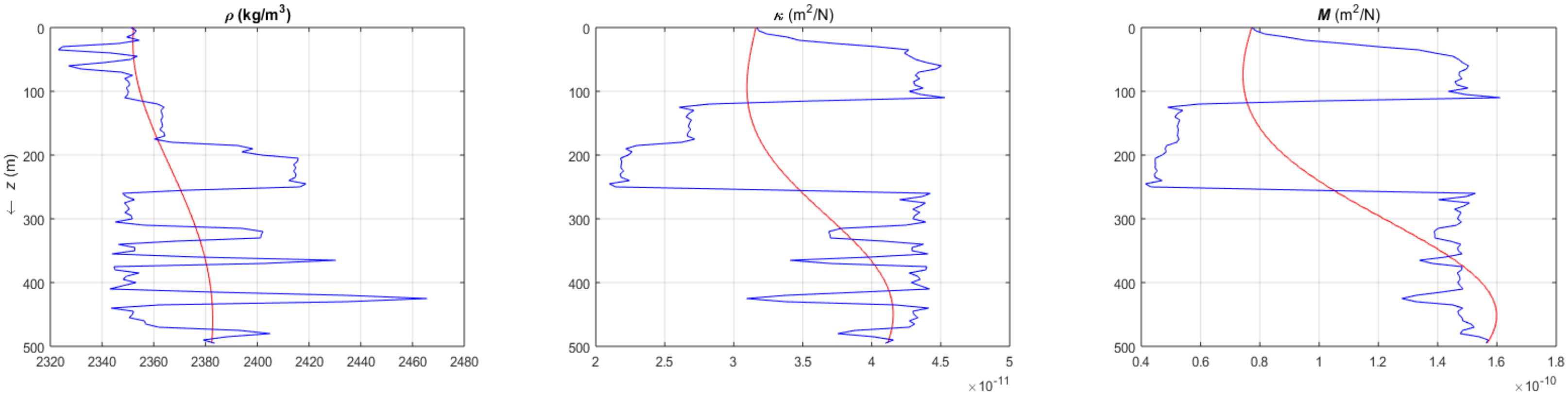

Figure 19: Property profiles for the synthetic data for common midpoint (CMP) 400. The red lines represent *a priori* background data which have been anti-alias filters for 5 m sampling.

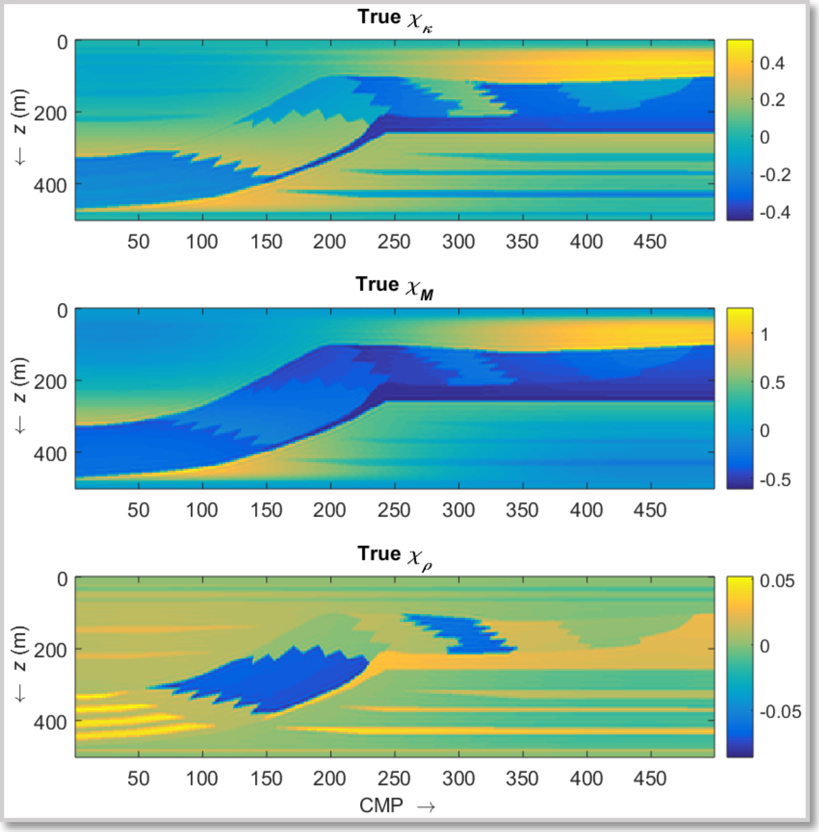

Figure 20: Contrasts of compressibility, $\chi_\kappa(z)$, shear compliance, $\chi_{\mathrm{M}}(z)$, and density, $\chi_\rho(z)$, are calculated to allow for linearization during the inversion process. These three matrices are what will be inverted in the FWI-res scheme.

Using the backgrounds from Figure 18, the true contrasts $\chi_\kappa(z), \chi_{\mathrm{M}}(z), and\ \chi_\rho(z)$ are calculated before the inversion process and are the values which will be inverted as previously mentioned. They can be seen in Figure 20 to the left.

Figure 21 illustrates the entire flow chart for the FWI-res process representing an inner and outer loop which uses the forward model, background models, and property contrasts for a set number of iterations. After each iteration the estimate of the total field is updated with every iteration trying to “fit” closer to the true parameters than previously before until the inversion is complete.

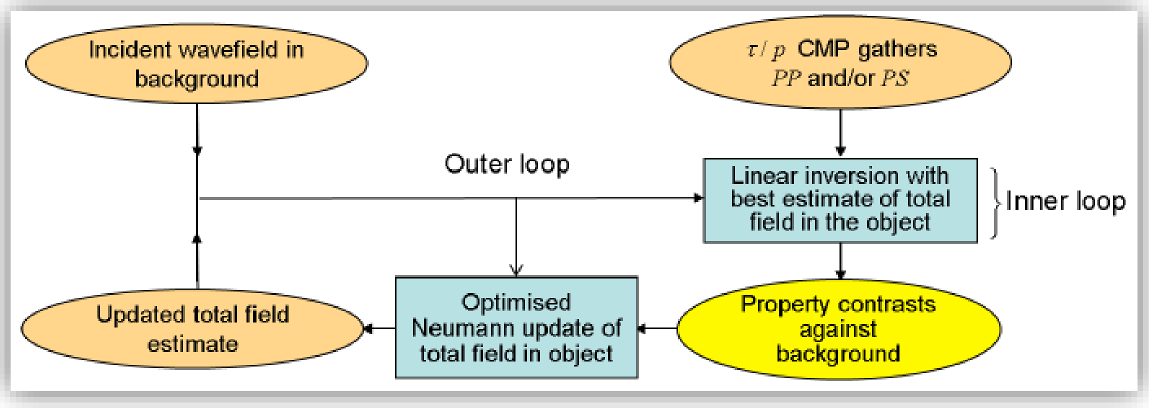

Figure 21: Flowchart for non-linear full-waveform inversion for reservoir characterization created by Veeken et al. (2014).

However, it should be noted that this deterministic method of matching a “best fit” curve to the data which is derived from porosity/velocity relations ought to be used with caution when inverting for carbonates. Eberli et al. (2003) warns that when using these inversion methods, the large scattering of values which were seen on Figure 3 (Ch. 1.2) will inadvertently result in large uncertainties (under or overestimation) in the inversion. This weak relationship between porosity and velocity in carbonates is caused by the ability of carbonates to form cements and special fabrics with pore types that can enhance the elastic properties of the rock without filling all the pore space (Eberli et al., 2003).

5.1 Inversion Results

After running 24 iterations for each CMP of the synthetic seismic data, the non-linear inversion results for CMP 400 are revealed in Figure 22 as an example. The true contrast values, $\chi_\kappa(z), \chi_\mathrm{M}(z), and\ \chi_\rho(z)$, are represented in red lines with the predicted total field is in blue. The top three plots of Figure 22 are raw inversion results without spatial filtering while the bottom three are bandpass-filtered from broadband back to the seismic bandwidth.

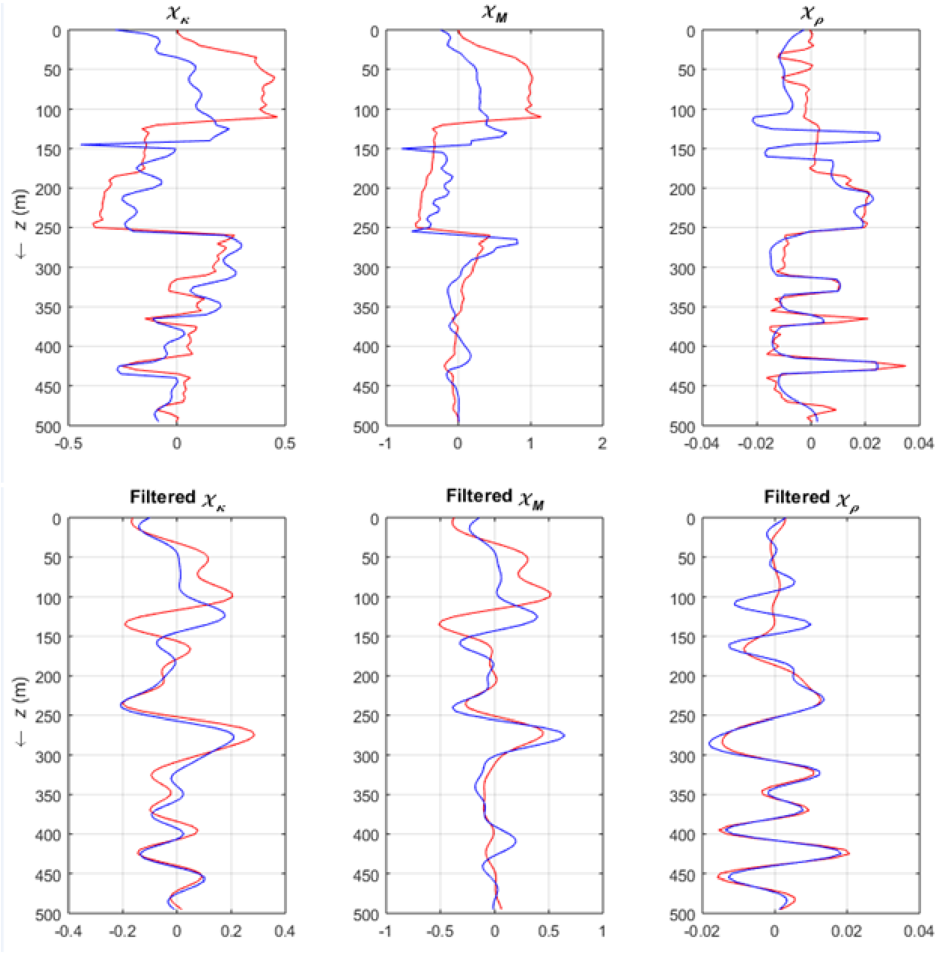

Figure 22: Result plots of 24 full-waveform inversion (FWI-res) iterations of one gather (CMP 400) for each contrast: compressibility, $\chi_\kappa(z)$, shear compliance, $\chi_M(z)$, and bulk density, $\chi_\rho(z)$. The true contrasts are depicted in red while the predicted inversion are in blue. The top three plots are the raw inversion while the bottom three a spatially filtered back to seismic bandwidth.

The purpose of bandpass filtering is to pass a certain bandwidth with little or no modification while largely suppressing the remaining parts of the frequency spectrum. It is a simple application of Fourier frequency analysis in the design of zero-phase filters to get rid of the high and low frequencies – thus brining the broadband exploited during non-linear inversion back to the seismic bandwidth (Yilmaz, 1987).

Even though $\chi_\kappa(z), \chi_M(z), and\ \chi_\rho(z)$ are what were inverted, for display purposes these contrasts have been converted back into compressibility (κ), shear compliance (M), and bulk density (ρ). The results are displayed in Figure 23Figure 24, and Figure 25 on the next page.

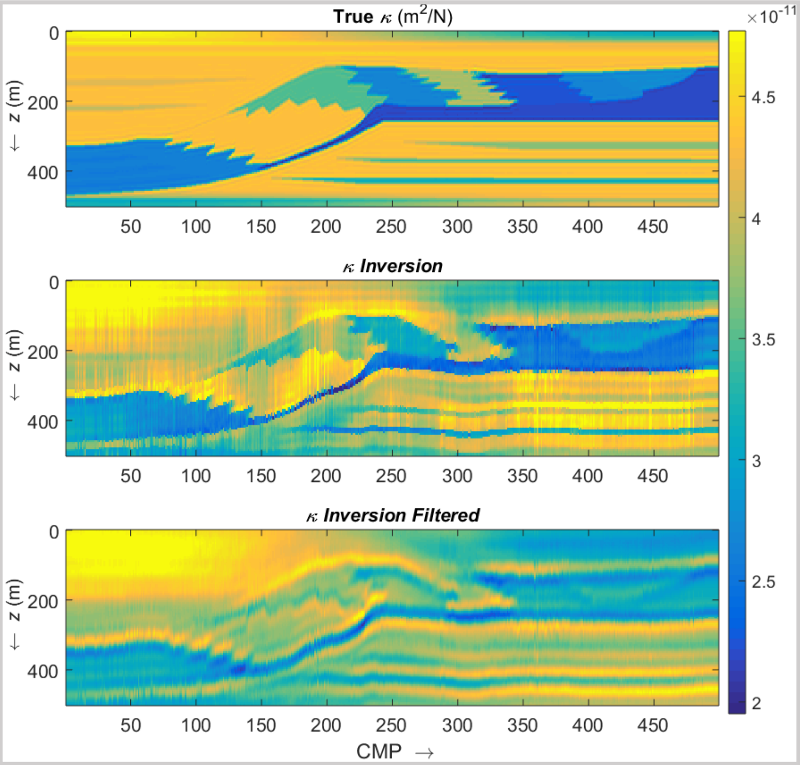

Figure 23: Full-waveform inversion (FWI-res) results of compressibility (κ) with the real values (top), predicted inversion (middle), and the inverted values spatially filtered back to seismic bandwidth (bottom).

Figure 24: Full-waveform inversion (FWI-res) results of shear compliance (M) with the real values (top), predicted inversion (middle), and the inverted values spatially filtered back to seismic bandwidth (bottom).

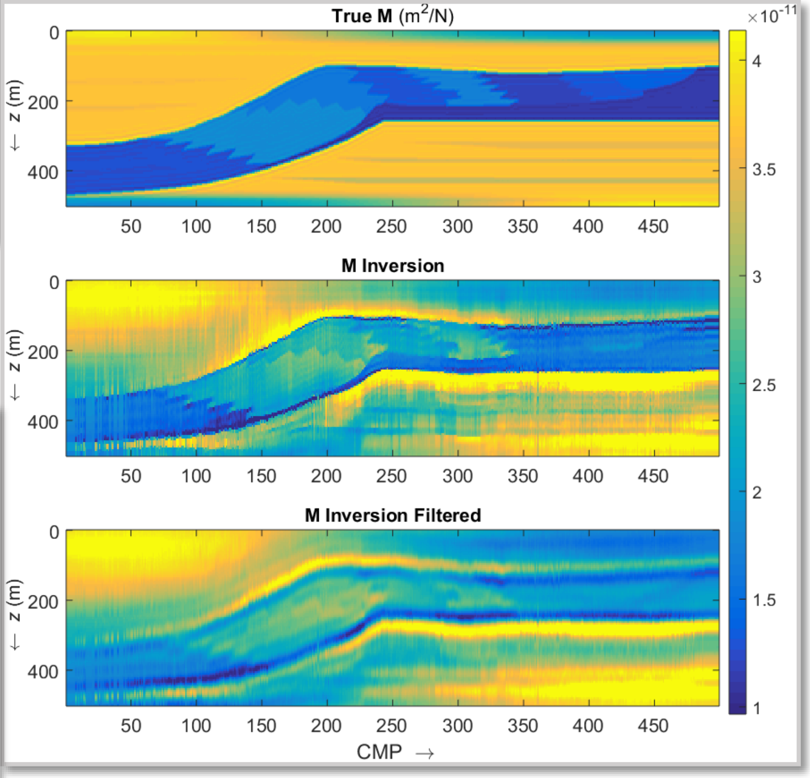

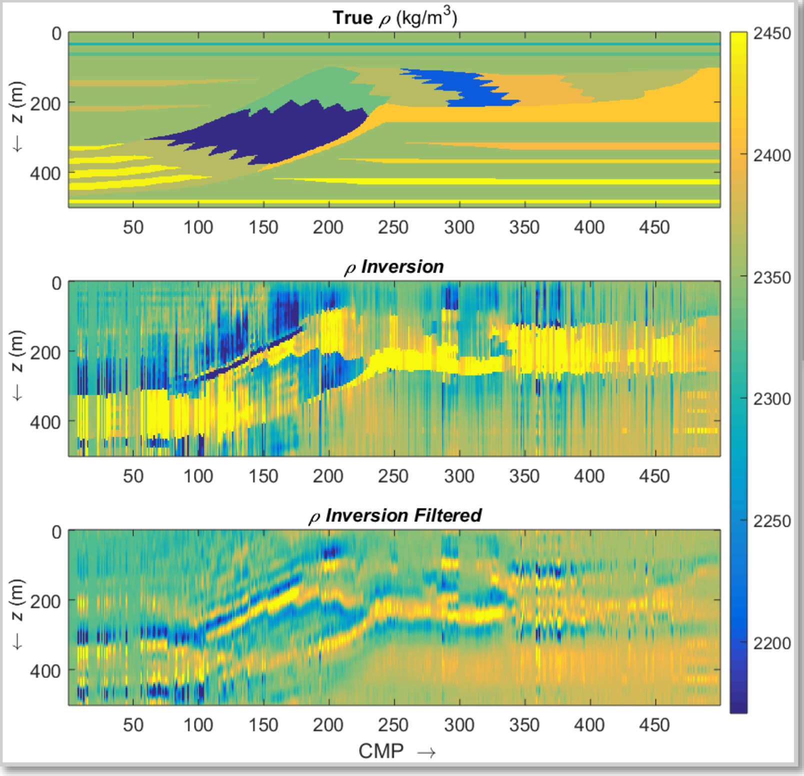

Figure 25: Full-waveform inversion (FWI-res) results of bulk density (ρ) with the real values (top), predicted inversion (middle), and the inverted values spatially filtered back to seismic bandwidth (bottom).

Lastly, to display the results in P- and S-wave velocity the equations [4 & 5] from Chapter 5 were used to convert the elastic parameters back into seismic velocities as seen in Figure 26 and Figure 27.

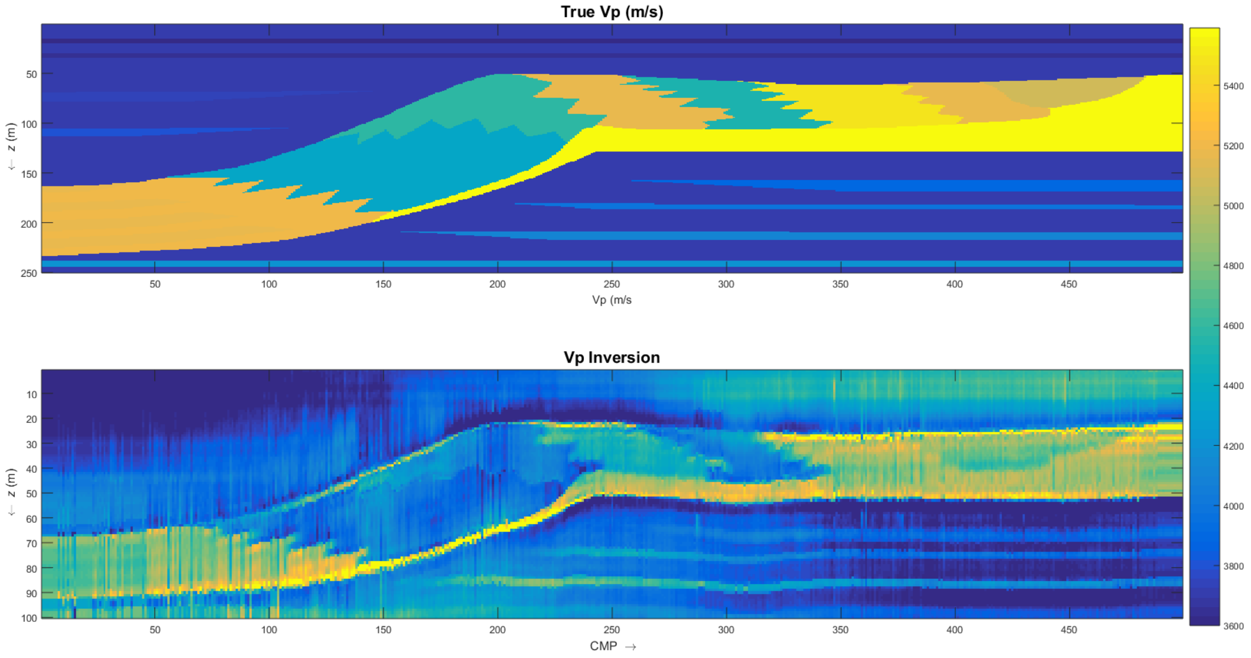

Figure 26: Full-waveform inversion (FWI-res) results of P-wave velocity (V_p) the real values (top) and predicted inversion (bottom).

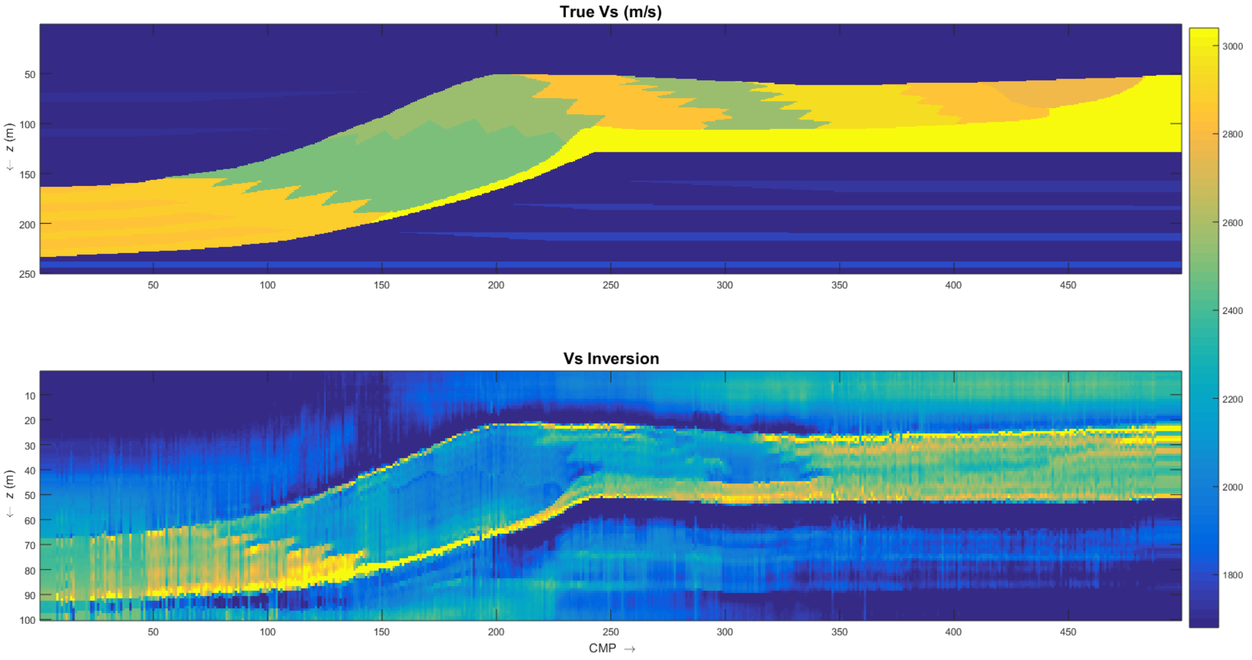

Figure 27: Full-waveform inversion (FWI-res) results of S-wave velocity (V_s) with the real values (top) and predicted inversion (bottom).

5.2 Inversion Evaluation

The inversion scheme worked quite well for this data set and was accurate in predicting the whole geometry of the carbonate ramp system. In addition, the inversion was fairly accurate in predicting the elastic model parameters of the different lithofacies. This can first be seen in Figure 22 of the results (Chapter 5.1) where the predicted inversion in blue is quite close to the true in red. When these inverted contrasts were eventually converted back to V_p and V_s (Figure 26Figure 27) one could realize that the average difference between the true values and the inverted values are around 430 m/s for both V_p and V_s.

However, not every CMP location had good inversion predictions for bulk density as is represented in Figure 22. It is believed that this is due to the inadequate density background (ρ_0) that was produced in Figure 18. Back in chapter 3 it was forewarned that there may be problems with inverting for bulk density due to not having laboratory density measurements for the samples and the weakness of equation [3]. The equation only calculated densities from porosity percentage and a common grain density – thus not having very much density variation between the different lithofacies types as there perhaps should have been. In addition, it ought to be comprehended that the FWI-res method is 1D and calculates trace by trace – mainly corresponding to large variations of the earth parameters and does not expect large lateral changes. (Gisolf et al., 2006). As was seen in Chapter 3 the geological model is relatively small scale (250 by 500 grid-space) with high contrasts in the lateral association of the different prograding carbonate facies. As such, the results of this inversion method perhaps were not as optimal as they could have been. So much so, that the bulk density prediction in Figure 25 could be considered completely un-usable seeing as the results had vertical ‘streaks’ within the data due to these high lateral changes. The streaks are not completely filtered away in the bandpass filter because of the method being 1D and thus filters vertically trace by trace rather than laterally.

Lastly, when seeking to relate the inverted elastic parameters to the different carbonate pore types, there is not enough uniform evidence to support any such correlation. The non-filtered inversion in Figure 23 shows a higher compressibility (κ) for all of the intergranular lithofacies as they should, but it also displays the two highest $\kappa's$ for the open moldic rudstone (~CMP 150) and the moldic back-reef (~CMP 325). As learned in the theory of Chapters 1.1 and 1.2 moldic carbonate lithofacies generally have more stiffness due to the heavily cemented framework and should thus show less compressibility in the inversion results. Similarly, in the non-filtered shear compliance (M) results of Figure 24 these same two moldic lithofacies (~CMP 150 and 325) display that they are highly susceptible to shearing which could again add confusion to the interpretation. As such, attempting to distinguish intergranular lithofacies from moldic/viggy ones would not be accurate enough with these inversion results. What one would notice though however, is that the lithofacies between CMP 100-350 on Figure 23-Figure 25 are distinguishable as a group on all inversion results.

6. Reservoir Characterization

After seismic inversion, the determination of lithofacies is a crucial problem in reservoir characterization and a prime factor in producing oil and gas in the E&P industry. As such, highly skilled experts are needed for the interpretation and evaluation of data. The primary task of geological and engineering characterization of petroleum reservoirs is to determine various lithofacies of the reservoir rocks. Therefore, designing a model that is able to determine lithofacies and classify important reservoir characteristics or stratigraphy using full-waveform inversion data without other information such as wireline logging would be extremely economical (Baneshi, 2014; Chikhi et al., 2004).

There is now enough quantitative information in this study describing each lithofacies to try and proceed with such lithology estimation, i.e., using the derived inversion values to try and determine which type of rock the data belongs to. One should theoretically ask, if someone were given only the inversion results of Chapter 5.1 without the true earth parameters would he be able to determine exactly the different types of lithofacies without relying on the distinctive geometries present? In this chapter, elementary lithofacies determination techniques will be carried out in hopes of matching the true lithofacies and their pore-types to the unknown lithofacies of the inverted results.

First, the intrinsic values gathered from each facies during the multi-parameter inversion can be combined using 2D and 3D (2 and 3 variable) crossplots to help identify the various units in the sedimentary structure. In the interest of plotting these values for each of the 10 facies (see Figure 28 below for numbering), a 5x15 matrix was selected within each facies for each parameter ($\kappa, \mathrm{M}, \rho, V_p, and\ V_s$). Of this, each set of 75 values for every parameter had its mean calculated as to represent the average value for the entire facies. In addition to these parameters, the true and inverted Poisson’s ratio will be plotted against M. For a review of elastic moduli including Poisson’s ratio, refer to the theory in sub-chapter 1.2. It should be noted though that most crustal rocks have Poisson’s ratios between about 0.2 and 0.3 (Ghose, et al., 2013).

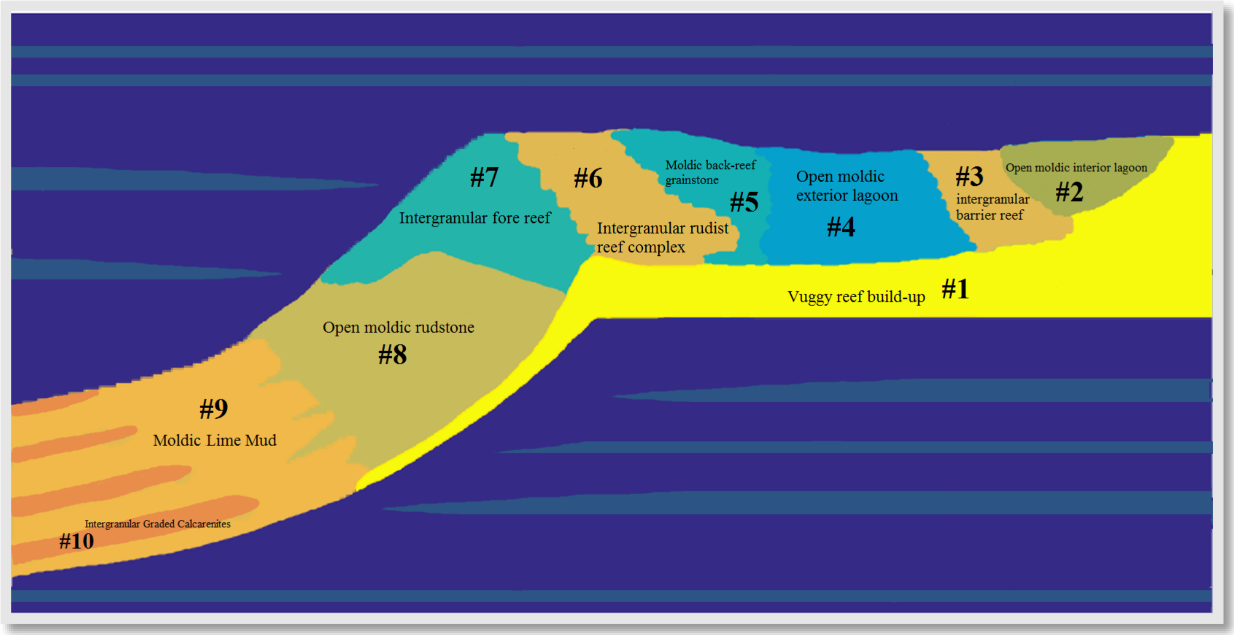

Figure 28: Geological model to represent the numbering system applied to cross-plotting of the intrinsic values gathered from inversion process (FWI-res). Additionally, each unit has a facies and pore type description.

After creating the crossplots with both the averaged true and inverted parameters, the method of Standardized Euclidean Distance is used to calculate the closest distance to a true value point (x_s) for each inverted value point (x_t). The hope is that the inverted facies will match with its true facies because in a perfect inversion this would be the case. The averages of the true $\kappa\ and$ M values were selected in the same manner of picking a 5x15 matrix within each facies while the true $V_p, V_s, and\ \rho$ had only homogeneous values for each facies. Euclidean Distance is defined as the square of the difference in each dimension (parameter) and the square root of the sum of these squared differences. This Euclidean Distance equation $\left(\sqrt{\sum(x_s - x_t)^2}\right)$ is represented in Matlab by $(x_s - x_t)(x_s - x_t)'$. For Standardized Euclidean Distance the distance is so-called standardized because each coordinate difference is scaled by dividing by the corresponding standard deviation. The equation for Standardized Euclidian Distance is represented by $d^2{}_{st}$ below

$$d^2{}_{st} = (x_s - x_t)V^{-1}(x_s - x_t)' \qquad [10]$$

where V^{-1} is a matrix containing the standard deviations (MathWorks, 2015).

6.1 Results

In Figure 29 and Figure 30 are the crossplot results of the true averages in blue and the inverted averages in green. Figure 29 is enlarged and the points are labeled to give the reader an initial representation of the 10 different facies locations and their vicinities from one another.

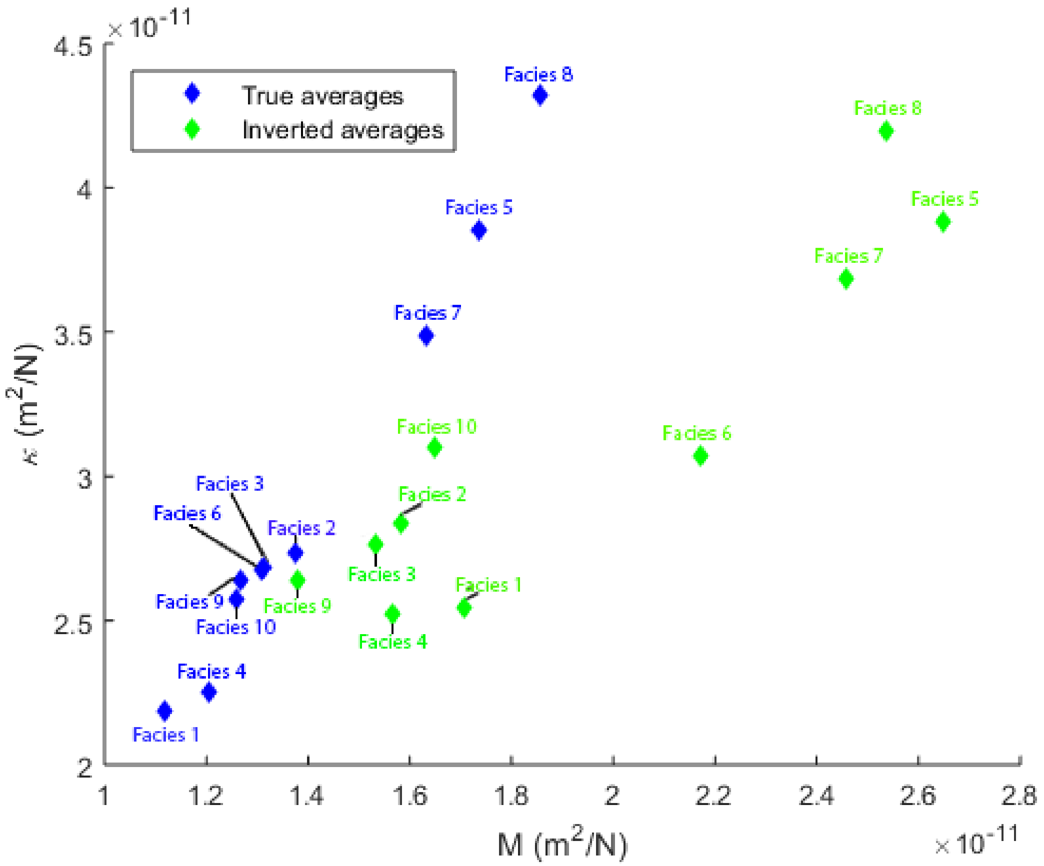

Figure 29: Compressibility (κ) versus shear compliance (M) crossplot with the true facies averages represented in blue diamonds while the inverted averages are green diamonds. The facies have been numbered according to the geological model of Figure 28.

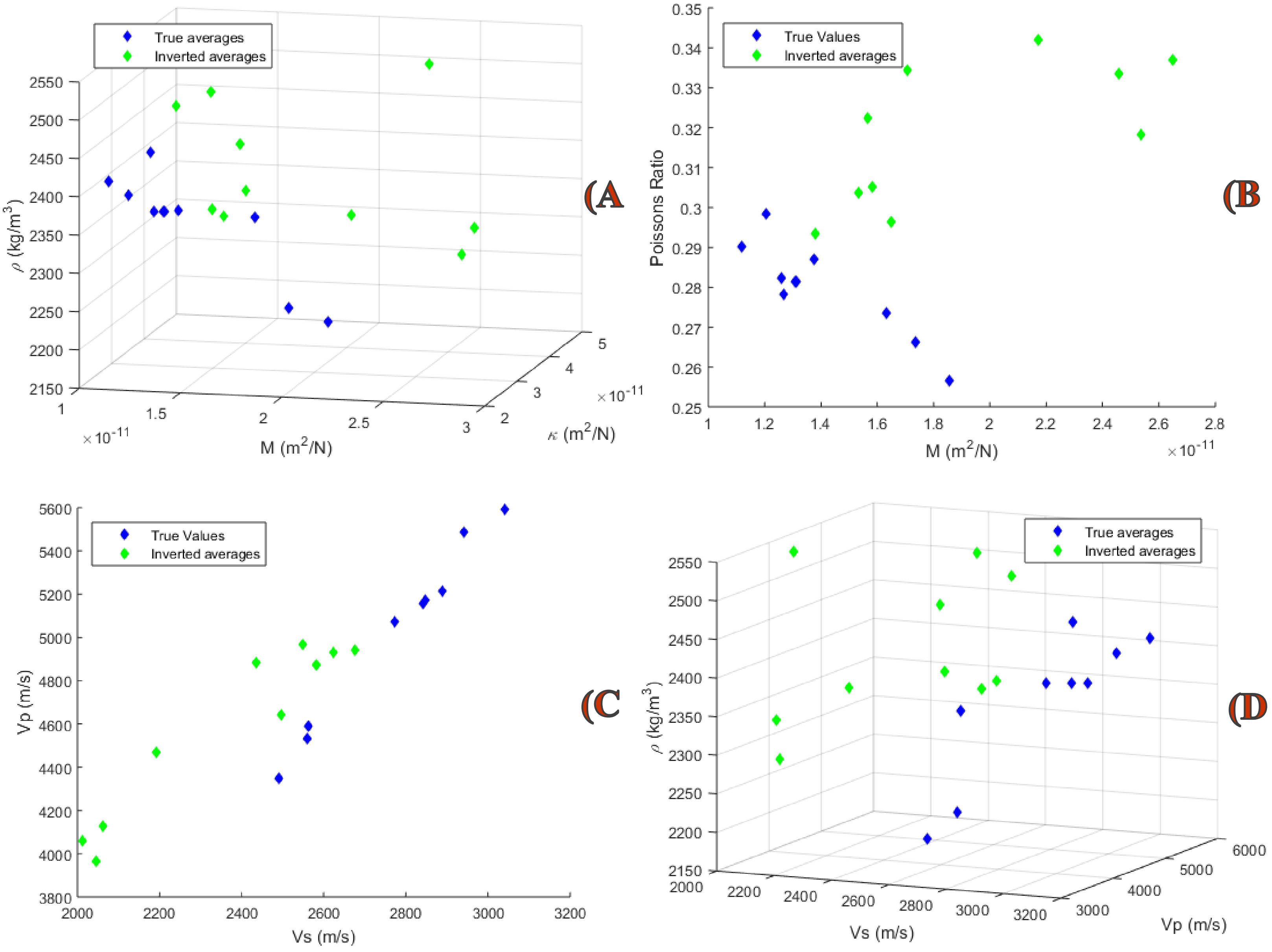

Figure 30: Two 2D crossplots (**B, C**) and two 3D crossplots (**A, D**) of various elastic parameters with the true average of each facies represented by blue diamonds while the inverted averages are green. The top left crossplot (**A**) is density (ρ) vs. shear compliance (M) vs. compressibility (κ) while the top right (**B**) is Poisson's ratio vs. M. The two crossplots on bottom are P-wave velocity (V_p) vs. S-wave velocity (V_s) (**C**) and ρ vs. V_p vs. V_s (**D**).

In Table 2 are the numerical results of the Standardized Euclidean algorithm where each facies number represents a green inverted facies point and a corresponding blue facies which it is closest to.

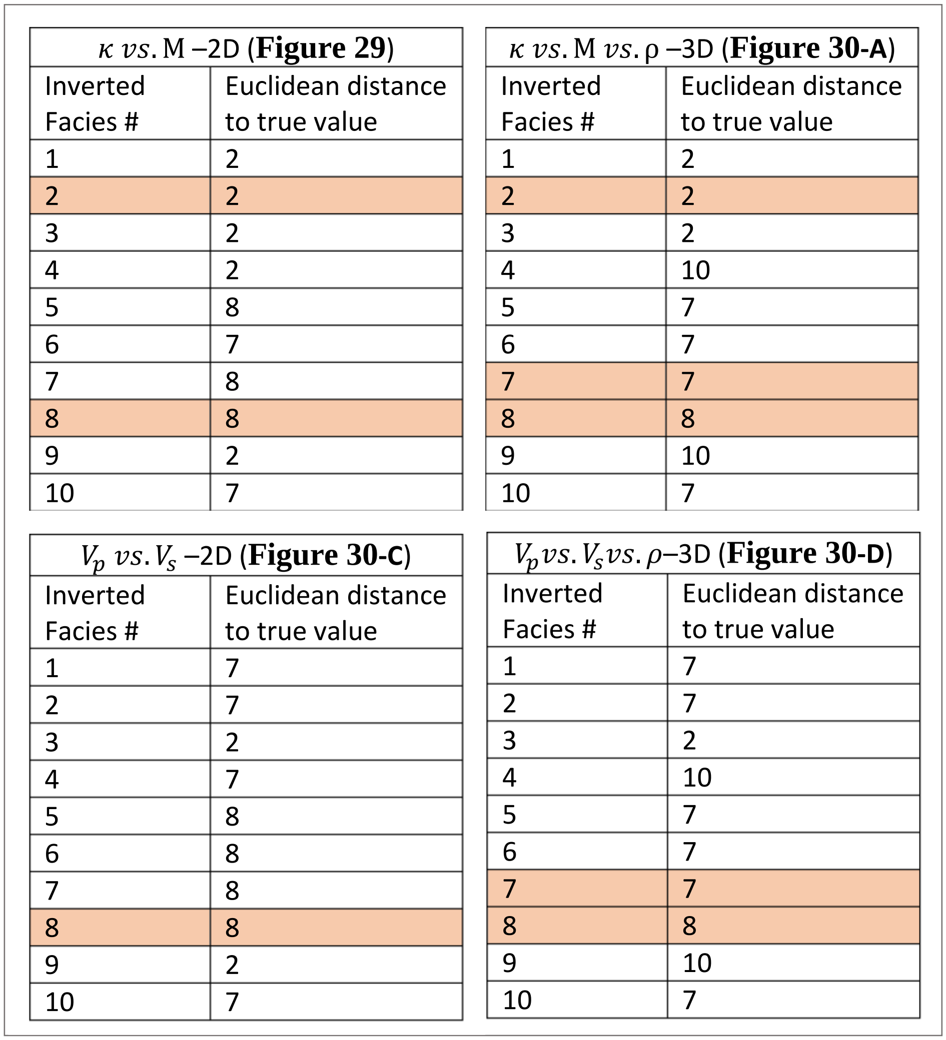

$\kappa\ vs.\ \mathrm{M}$ –2D (**Figure 29**)

Inverted Facies #	Euclidean distance to true value
1	2
2	2
3	2
4	2
5	8
6	7
7	8
8	8
9	2
10	7

$\kappa\ vs.\ \mathrm{M}\ vs.\ \rho$ –3D (**Figure 30-A**)

Inverted Facies #	Euclidean distance to true value
1	2
2	2
3	2
4	10
5	7
6	7
7	7
8	8
9	10
10	7

$V_p\ vs.\ V_s$ –2D (**Figure 30-C**)

Inverted Facies #	Euclidean distance to true value
1	7
2	7
3	2
4	7
5	8
6	8
7	8
8	8
9	2
10	7

$V_p vs. V_s vs. \rho$–3D (**Figure 30-D**)

Inverted Facies #	Euclidean distance to true value
1	7
2	7
3	2
4	10
5	7
6	7
7	7
8	8
9	10
10	7

Table 2: Four seperate tables of the Standardized Euclidian Distance results taken from four different crossplots. The top left table is from Figure 29 while the other three are the results of A, C, and D from Figure 30. The first column of each table represents the inverted average points (green diamonds from the figures) and the second column represents the true average point which is within the closest vicinity. The rows which are peach colored represent the only inverted facies to exactly match its true counterpart.

7. Discussion

As seen in the results of the inverted crossplots and Standardized Euclidean Distance in Chapter 6.1, the lithofacies determination does not match up accurately enough to distinguish each facies individually as was anticipated. Even though Table 2 shows two or three matches for each crossplot, the majority of inverted facies still do not have unique matches. For example, the Euclidean distances calculated for Figure 29 in Table 2 has the true facies “#8” unexclusively matching to 3 different inverted facies of the ten total. As a consequence, even though we know the inverted facies #8 matched with the true facies #8, if the different facies types were not known prior to using this method it would be too difficult to differentiate which inverted facies actually belong to facies type #8. In other words, although inverted facies #8 made a correct match there would be no way to determine if it actually was correct or not since two other inverted facies also matched facies #8 (incorrectly). This circumstance is crucial due to facies #8 and #7 (which also had an exact match in two iterations) being a couple of the main targets of interest for oil production. Therefore the Standard Euclidean Distance calculations were not very successful and the different lithofacies types cannot completely be distinguished. However, the good news to these results is that even though facies #7 and #8 were not completely differentiated, they were still in fact matched to their true counterpart in most cases. Not only were they correctly matched, but the facies in close spatial proximity to #7 and #8 on the geological map also matched to either facies #7 or #8. This can be seen in Table 2 where inverted facies #5, #6, #7, and #8 were consistently matched to either facies #7 or #8. This is a significant finding which supports the notion that these four facies (the four main facies of interest in regard reservoir properties due to high permeability) share enough in common to incorrectly be matched with each other.

As determined, if the true earth parameters are not known prior to crossplotting, the ten different lithofacies cannot be differentiated individually. Subsequently, focus shifts to another aspect of the crossplots—that is observation of the peculiarities regarding how inverted lithofacies are clustered. Cluster investigation is a tool for data integration analysis used by geoscientists to distinguish data which share the same characteristics (Marroquín, 2015). This specific study intends to use inverted seismic attribute patterns to differentiate seismic facies and to eventually enable others to use the method without *a priori* information.

Since the intention then is no longer to differentiate each lithofacies individually, the ten lithofacies types have been subdivided into three facies groups in order to help with the cluster investigation. These three facies groups are the groups known from the geological model created in Chapter 3: (i) lagoon and barrier reef; (ii) back-reef/core-reef complex/fore-reef-slope; and (iii) deep sea basin. Figure 31 (A) below shows the base geological model remade into a facies group map by assigning a color to each facies group and then filling in each of the ten facies with its corresponding facies group color. Figure 31 (A) also denotes which individual facies are included in each facies group. Figure 31 (B) is that same method of color coding but converted onto the M inversion results taken from Figure 24 to represented how it translates to the actual results.

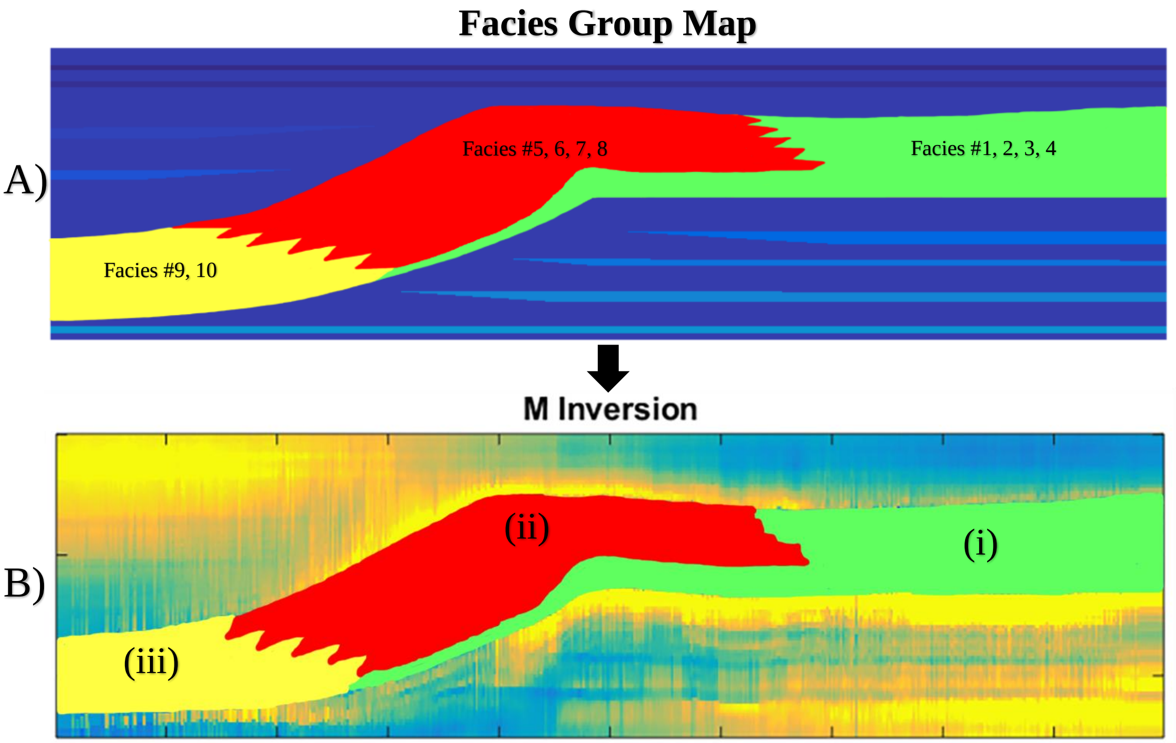

Figure 31: Facies map **(A)** color coded by the three different facies groups: (i) lagoon and barrier reef in green; (ii) back-reef/core-reef complex/fore-reef-slope in red; and (iii) deep sea basin in yellow. The color coded facies map has been translated onto the shear compliance (M) inversion results **(B)** to represent what the interpreter would be working with.

As represented in the κ versus M crossplot (Figure 29), since the true parameters are known, the ten different inverted lithofacies can be located on the crossplots. Figure 32 below is the same crossplot as Figure 29 with the exception that it only depicts all inverted lithofacies without the true values. Figure 32 (A and C) shows all 750 data-points plotted while the other (B and D) shows the ten averages.

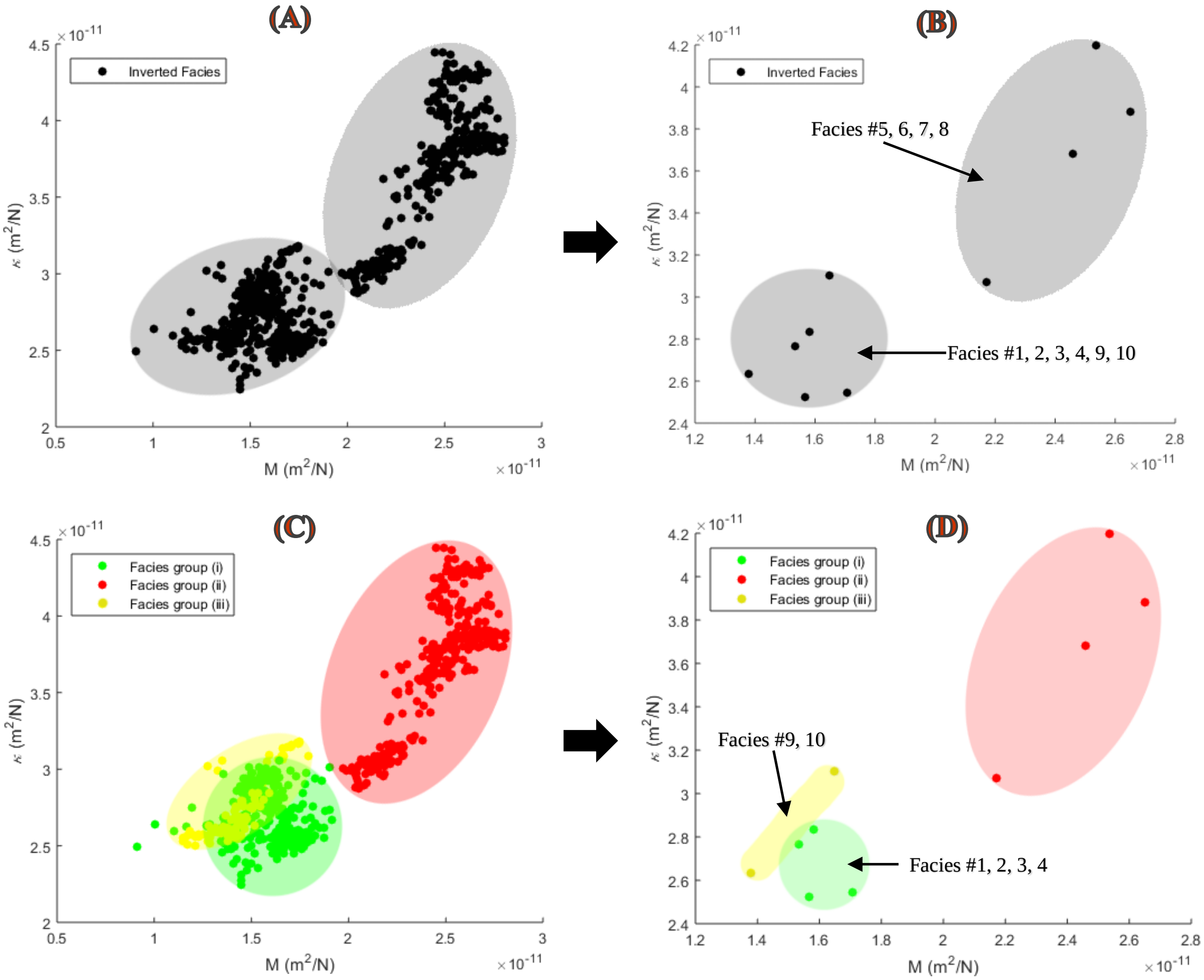

Figure 32: 2D crossplots of data-points extracted from ten different lithofacies within the compressibility (κ) and shear compliance (M) inversion results. Plots **A** and **C** contain 750 of the extracted data-points while **B** and **D** represent the average value for each facies. Plots **A** and **B** have two apparent clusters shaded in grey while **C** and **D** have three clusters color coded based on their facies groups: (i) lagoon and barrier reef in green; (ii) back-reef/core-reef complex/fore-reef-slope in red; and (iii) deep sea basin in yellow. The facies are numbered based on the Figure 28 model.

Figure 32 (A and B), which portray uncategorized lithofacies, depict that there are only two apparent clustered facies groups that are shaded in grey even though there were three facies groups as defined in Figure 31. This is explained by Marroquín (2015) in his data integration study where he states that there are major issues which affect the validity and quality of seismic facies clustering results. One of these issues is the choice of the optimal number of facies to cluster. He explains that the appropriate choice of this number balances the accuracy of sample points assigned to their own groups versus the number of groups to be detected. For example, if there are too few seismic facies groups, different sample inputs can be incorrectly merged into a single group. As a result, facies groups are less compact due to inappropriate mixing of individual inputs. Likewise, if there are too many seismic facies groups, homogeneous clusters can be improperly split into several groups. The result is that seismic facies groups are too close, causing little distinction between adjacent groups (Marroquín, 2015). As such, plots A and B are examples of the interpreter defining only two facies groups when in reality there should be three. Thus, facies group (i) and (iii) are perhaps incorrectly merged into one cluster in the scenario that a researcher would try this technique without using the depositional facies groups as defined in this study.

On the contrary (in plots C and D), the inverted lithofacies are color coordinated based on the three facies groups so that one may interpret three different clusters. In the plots with ten data-points (B and D), the distance between clusters has been maximized and are increasingly distinguishable. This suggests that having large amounts of data-points could end up leaving a bit of discrepancy when interpreting the clusters (A and C) and it is recommended that the average values be plotted for clustering inverted parameters. This is especially true when it comes to interpreting the overlapping clusters of the basinal facies group (yellow) and the lagoon/barrier reef facies (green) overlapping each other in plots C and D. When all 750 data-points are plotted it is arguable that these two facies groups would still not be distinguishable (plot C) but when the averages are clustered (plot D) the interpreter can recognize facies #9 and 10 as the basinal facies group.

The facies groups (i) and (iii) of plot A (Figure 33) can further be distinguished from each other by replacing κ with the Poisson's ratio (plot B) in which the Poisson's ratio acts as the z-axis of plot A. One can imagine the data-points of plot A literally extending into the plot to be what is seen on the y-axis of plot B. Thus the apparent overlapping of the yellow and green clusters in plot A is no longer present.

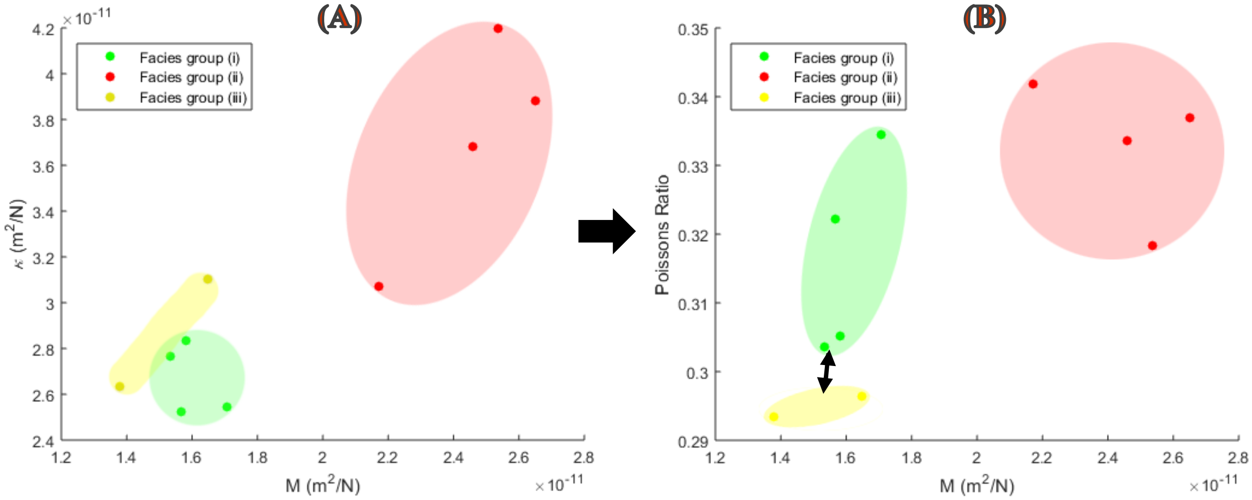

Figure 33: 2D crossplots of data-points extracted from ten different lithofacies within the compressibility (κ) and shear compliance (M) inversion results. Plots **A** and **B** have three clusters color coded based on their facies groups: (i) lagoon and barrier reef in green; (ii) back-reef/core-reef complex/fore-reef-slope in red; and (iii) deep sea basin in yellow. The apparent overlapping of facies group (i) and (iii) in plot **A** is no longer present in plot **B** which increased the distance between the two clusters (black arrows).

The 2D crossplot of V_p versus V_s (Figure 34) is quite similar in regard to clustering, as the previous crossplots (Figure 32 and Figure 33). The subtle difference is that the distance between facies group (ii) in red and the other two groups has increased on the y-axis as indicated by the black arrows.

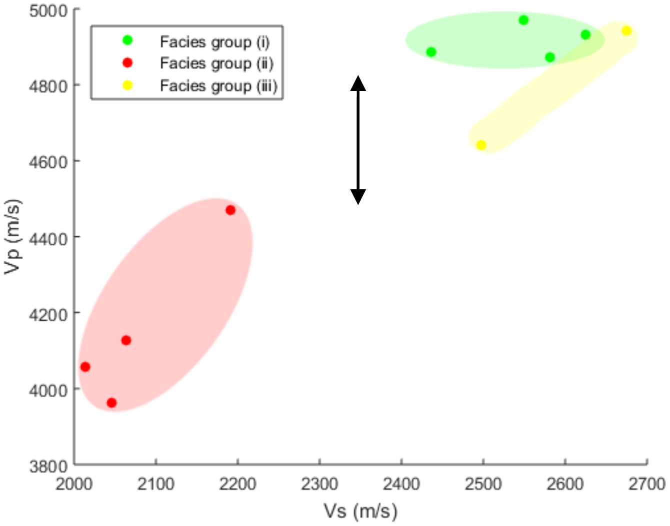

Figure 34: 2D crossplots of data-points extracted from ten different lithofacies within the P-wave velocity (V_p) and S-wave velocity (V_s) inversion results. The plot has three clusters color coded based on their facies groups: (i) lagoon and barrier reef in green; (ii) back-reef/core-reef complex/fore-reef-slope in red; and (iii) deep sea basin in yellow. The vertical arrow indicates the increased separation on the y-axis of the red cluster from the rest.

Figure 35 below contains 3D plots of ρ versus κ versus M. Plots A and B are not notably better for distinguishing the clusters as compared to the 2D plots (Figure 32, Figure 33, and Figure 34) but displaying both gives the reader a different perspective.

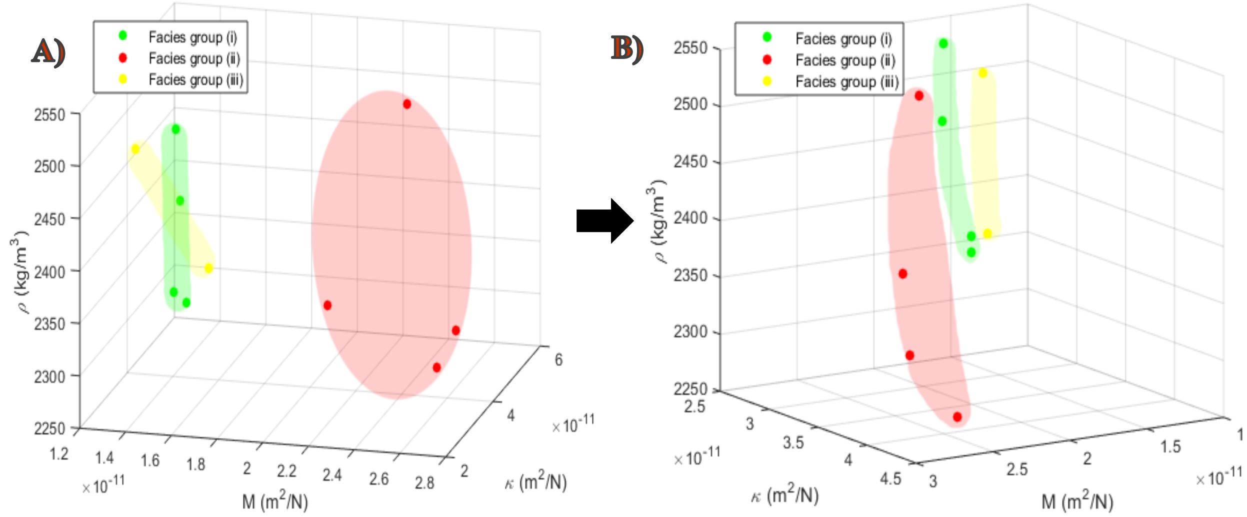

Figure 35: 3D crossplots of data-points extracted from ten different lithofacies within the compressibility (κ), shear compliance (M), and bulk density (ρ) inversion results. The plots depict three different clusters: (i) lagoon and barrier reef in green; (ii) back-reef/core-reef complex/fore-reef-slope in red; and (iii) deep sea basin in yellow. Plot **A** and **B** are the exact same with the exception that **B** shows more of a "side" view of the clusters to illustrate that the clusters are indeed separate

8. Conclusions

This study sought to answer whether or not various types of carbonate lithofacies could be differentiated based on the characterization of their pore types through the use of full-waveform reservoir inversion (FWI-res). To accomplish this task, various non-saturated carbonate reservoir rocks were embodied in a 500 m by 12.5 km theoretical geological model using limestone samples gathered by Fournier et al. (2014). The model represented a marine carbonate shelf with a fore-reef slope system and upon its completion a forward model simulation was carried out using the Kennett invariant embedding method (Kennett, 1983) with a zero-phase wavelet which utilized frequencies between 6 and 75 Hz. After observing that there were no unique seismic indicators on the forward model that led to any interpretation of different lithofacies types, the forward model was put into an inversion algorithm developed by Gisolf and van den Berg (2010) in an attempt to quantitatively recreate the geological model. Using the derived elastic parameter values predicted from inversion, the different facies were gathered into 2D and 3D crossplots. Within the various crossplots, ranging from compressibility (κ) vs. shear compliance (M), the Poisson's ratio vs. M, P-wave velocity (V_p) vs. S-wave velocity (V_s), to bulk density (ρ) vs. κ vs. M, the data points were characterized based on their given cluster orientation.

In the end, the lithofacies determination was successful but not in the way initially theorized. The different pore-types did not play a significant role in characterizing the various clusters but instead it was found that settings of environmental deposition played as a substantial contribution. Instead of identifying each of the ten lithofacies (defined by the geological model), three lithofacies groups were able to be determined using only the seismic data. The facies groups were found based on environments of deposition, specifically: lagoon and barrier reef; back-reef/core-reef complex/fore-reef-slope; and deep sea basin.

Although pore-types of different carbonate lithofacies which are critical to determine for petroleum production lie outside the grasp of seismic inversion characterization, the cluster characterization method as used in this study can be replicated using only surface-seismic full-waveform inversion data to classify a reservoir rock's origin of environmental deposition. This indeed still has significant implications as it puts exploration and production companies one step closer to having alternative options other than borehole data such as wireline logging to characterize and determine carbonate reservoir lithofacies suitable for production. Furthermore, any researcher who is given a surface-seismic dataset without much *a priori* information of the subsurface can characterize the post-full-waveform inversion data based on the cluster orientation of the three facies groups as defined in this study. If said researcher were to not use the three depositional facies groups, there could be a lithofacies type that goes undetected by different sample inputs being incorrectly merged into a single group.

8.1 Recommendations

It is recommended if this research method is replicated that the researcher plot the inverted data by the Poisson's ratio versus shear compliance to first attempt distinguishing the different clusters. This is due to the fact that during this study the Poisson's ratio vs. shear compliance crossplot displayed the least amount of discrepancy as it had the largest distance between the three facies group clusters. In addition, it is recommended to replicate the entire experiment without using dry carbonate samples and instead include saturation densities. Not only will the experiment more-so resemble a hydrocarbon reservoir by accounting for brine and hydrocarbon saturations, but it could also improve the inversion results by providing more variation in bulk densities. To do so, a completely new carbonate dataset with both laboratory density measurements and saturated velocity measurements will have to be attained. Gassmann's fluid substitution (1951) does not work optimally enough with carbonate rocks which gives reason for why the dataset must be obtained. The (Gassmann's) theory models fluid effects on rock velocity and density as described on Petrowiki.org. If the fluid substitution did work for carbonates, this study would have applied Gassmann's equation to adjust the P- and S-wave velocities according to the modelled saturations and thus could have accounted for fluid saturations in the density calculations. However, it is said that Gassmann's theory assumes fluid does not chemically alter the mechanical properties of the solid matrix of the rocks (Baechle et al., 2005; Adam et al., 2006). While the theory does work well for sandstones, laboratory studies have been proven by Baechle et al. (2005) and Adam et al. (2006) that for carbonate samples shear moduli (μ) does not remain constant during saturation and therefore velocities predicted with the Gassmann equation can be 5% to 20% lower or higher than measured velocities. Adam et al. go on to explain that μ is particularly sensitive to brine saturation and that weakening of the solid matrix occurs possibly due to surface energy loss and/or subcritical crack growth in compliant pores. As such, when shear velocity encounters a saturated rock dispersion can occur or the shear wave can take a preferential propagation path which avoids weakened sections – thus violating Gassmann's assumption and making fluid substitution for carbonate inadequate (Adam et al., 2006).

Once a dataset with carbonate saturations and densities has been established, the next step to improving this study would be to recreate the geological model to resemble more of a progradational carbonate shelf system. This progradational model would have the various carbonate lithofacies that were present in this study overlapping each other with multiple carbonate shelves, thus producing more complex (and realistic) geologies for the forward model and inversion processes. This progradational model was not built in the current study due to the inability of including fluid saturations and formulating better bulk density values. Thus it was decided that due to this study focusing more on the inverted parameters and crossplotting but not seismic attributes, creating a new model would not aid in improving the inverted parameters/crossplots and would give similar values as the base model.

Lastly, if a dataset can be found (or laboratory measurements can be made) with carbonate mineral bulk moduli values, porosities could be calculated from the inversion results in order to help further research if distinguishing lithofacies based on pore-types is possible. There are empirical equations relating mineral bulk modulus to porosity found in "The Rock Physics Handbook" by Mavko et al. (1998).

References

Adam Ludmila, Batzle Michael and Brevik Ivar Gassmann's fluid substitution and shear modulus variability in carbonates [Journal] // Geophysics. - 2006. - Vol. 71 No. 6. - pp. F173–F183.

Anselmetti Flavio S. and Eberli Gregor P. Controls on Sonic Velocity in Carbonates [Journal] // PAGEOPH. - [s.l.] : Birkhaiuser Verlag, Basel , 1993. - Vols. 141, No. 2/3/4 .

Baechle Gregor T., Weger Ralf J., Eberli Gregor P., Massaferro Jose L., Sun Yue-Feng Changes of shear moduli in carbonate rocks: Implications for Gassmann applicability [Journal] // The Leading Edge. - May 2005.

Baneshi M. The Determination of Lithofacies Using an Optimized Neural Network and Well Log Data [Book]: Petroleum Science and Technology Vol. 32 Issue 8 – 2014

Chikhi S., Batouche M. Probabilistic neural method combined with radial-bias functions applied to reservoir characterization in the Algerian Triassic province [Journal]. – J. Geophys. Eng. Vol. 1 Num. 2 - 2004

Dix C.H. Seismic velocities from surface measurements [Journal]: Geophysics, 20, no. 01, 68-86. - 1995

Drijkonigen G. G. Introduction to Reflection Seismology [Report] : B.Sc. version / Applied Geophysics & Petrophysics ; Delft University of Technology. - 2009.

Eberli Gregor P., Baechle Gregor T., Anselmetti Flavio S., Incze Michael L. Factors controlling elastic properties in carbonate sediments and rocks [Journal] // The Leading Edge. - July 2003.

Fournier François, Leonide Philippe, Kleipool Luuk, Toullec Renault, Reijmer John J.G., Borgomano Jean, Klootwijk Thomas, Molen Jeroen Van Der Pore space evolution and elastic properties of platform carbonates (Urgonian limestone, Barremian-Aptian, SE France) [Journal]. - [s.l.] : Elsevier B.V. , 2014. - Sedimentary Geology 308. - pp. 1-17.

Ghose Ranajit, Drijkoningen Guy and Slob Evert Methods of Exploration Geophysics [Report] : Lecture notes, AES1501 / Geoscience and Engineering ; Delft University of Technology. - 2013.

Gisolf A., van den Berg P.M. Target Oriented Non-linear Inversion of Seismic Data. EAGE Extended Abstract P. 308 – EUROPEC – 2010

Gisolf Dries, Rizzuti Gabrio Elastic wave-field inversion of seismic reflection data for high-resolution near-surface characterization – SEG Denver P. 2066 - 2014

Harbaugh John W. Developments in Sedimentology [Book]. - 1967. - Vol. 9 Part A.

Haffinger Peter, Doulgeris Panos, Gisolf Dries Delft Inversion – Retrieved from http://www.delft-inversion.com - 2015

Haffinger Peter Seismic Broadband Full Waveform Inversion by shot/receiver refocusing [Report] : Ph.D. Thesis, Delft University of Technology - 2013

Kennett B.L.N. Seismic Wave Propagation in Stratified Media [Book]: Cambridge University Press – 1983

Lam C.H., Bukrac S., van den Berg P.M., Gisolf A. On the background model for non-linear inversion of seismic data – SEG New Orleans P. 2012 - 2006

Lønøy Arve Making sense of carbonate pore systems [Journal] // AAPG Bulletin. - 2006. - Vol. 90.

Marroquín Iván Dimitri Automated seismic facies for data integration: an example from Fort Worth Basin, Texas (USA) [Journal] // First Break vol. 33 – May 2015.

MathWorks Pairwise distance between pairs of objects [Online] - http://nl.mathworks.com/help/stats/pdist.html – 2015

Maurer Hansruedi Inverse Theory for Geophysics I: Basics [Report]: Lecture Script, Institute of Geophysics, ETH Zürich – 2014.

Nurmi Roy and Standen Eric Carbonates, the inside story [Online]. - Schlumberger , 1997. - http://www.slb.com/~/media/Files/resources/mearr/wer18/chapter2.pdf.

Schlumberger Carbonate Reservoirs [Online] // www.slb.com/carbonates. - 2007.

Scholle Peter A., Bebout Don G. and Moore Clyde H. Carbonate Depositional Environments [Book]. - 1983. - Vol. AAPG Memoir 33.

Sirgue Laurent Inversion de la forme d'onde dans le domaine fréquentiel de données sismiques grands offsets [Report] : Thése de Doctorat de l'Université Paris XI - 2003

Soete J., Kleipook L.M., Claes H., Hamaekers H. Kele S., Ozkul M., Foubert A., Reijimer J.J.G., Swennen R. Acoustic properties in travertines and their relation to porosity and pore types [Journal] // Marine and Petroleum Geology. - 2014. - 59. - pp. 320-335.

Tetyukhina Daria High-resolution reservoir characterization by seismic inversion with geological constraints [Report] : Ph.D. Thesis, Delft University of Technology - 2010

Tetyukhina Daria, Luthi Stefan M., Gisolf Dries Full elastic seismic data modeling of an outcrop-based high-resolution geological and petrophysical model, Book Cliffs (Utah, USA). : SEG San Antonio – 2011

Tetyukhina Daria, Luthi Stefan M., Gisolf Dries Acoustic nonlinear full-waveform inversion on an outcrop-based detailed geological and petrophysical model (Book Cliffs, Utah). : AAPG bulletin, v. 98, No. 1 P. 119-134, January – 2014

Veeken P.C.H, Gisolf A., Huis in't Veld R., Haffinger P., Hanitzsch C., Doulgeris P. Non-linear Full Wavefield Inversion Applied to Carboniferous Reservoirs in the Wingate Gas Field (SNS, Offshore UK) – 76th EAGE conference & Exibition, Amsterdam – June, 2014

Weltje Gert Jan Carbonates 2 [Analysis of Sedimentary Data lecture slides] – TU Delft : , 2013

Yilmaz Özdogan Seismic Data Processing [Book]: SEG - 1987